The Dissertation Committee for Cynthia Elizabeth Correa
certifies that this is the approved version of the following dissertation:

Studies of Transient Behavior and of the Unbounded Magnetized Plasma Jet Configuration in the Magnetohydrodynamic Regime

Committee:

Herbert Berk, Supervisor

Roger Bengtson

Wendell Horton

Milos Milosavljevic

Linda Reichl

Studies of Transient Behavior and of the Unbounded Magnetized Plasma Jet Configuration in the Magnetohydrodynamic Regime

by

Cynthia Elizabeth Correa, B.A.

DISSERTATION

Presented to the Faculty of the Graduate School of

The University of Texas at Austin

in Partial Fulfillment

of the Requirements

for the Degree of

DOCTOR OF PHILOSOPHY

THE UNIVERSITY OF TEXAS AT AUSTIN

May 2015

Dedicated to my mother: the wonder woman who, through her talent, grit, and immense love, has carved out of this uncertain world, a steadfast and heartening home.

Acknowledgments

I wish to thank my research advisor, Dr. Horton, for enthusiastically supporting me at every step, and generously providing his time and knowledge, thereby making my graduate studies a very formative and enriching experience.

I thank Dr. Berk for going beyond his adoptive advisor duties with his friendly and wise guidance.

I thank my group mates Ehab Hassan, Jingfei Ma and Dmitry Meyerson for their ever cordial and cheery dispositions.

Studies of Transient Behavior and of the Unbounded Magnetized Plasma Jet Configuration in the Magnetohydrodynamic Regime

Cynthia Elizabeth Correa, Ph.D.
The University of Texas at Austin, 2015

Supervisor: Herbert Berk

Two studies with analytical and computational components of dynamics of plasmas and electromagnetic fields in the magnetohydrodynamic (MHD) regime are carried out to explain important and novel results from two laboratory plasma experiments. The first study provides a possible mechanism to explain transient magnetic fluctuations observed in the Large Plasma Device at the University of California - Los Angeles [Gekelman, 1991] and shows good qualitative agreement with the experimental results. The calculations are based on the nonmodal approach, which recovers transient dynamics missed by the conventional spectral treatment of configurations with sheared flow. The second study demonstrates several effects of the presence of boundaries on the evolution of a bounded magnetized plasma jet for the parameters and the configuration of the Helimak experiment at the University of Texas at

Austin [Gentle, 2008]. The bounded magnetized plasma jet is simulated with a Chebyshev-τ code. Both of these studies focus on time and length scales where the plasma is most adequately described by a resistive-viscous MHD model.

Table of Contents

Acknowledgments v

Abstract vi

List of Tables x

List of Figures xi

Chapter 1. Introduction 1
- 1.1 Generation of Alfvenic fluctuations in LAPD 1
- 1.2 Evolution of bounded jet 3

Chapter 2. Generation of Alfvénic fluctuations in sheared flow 5
- 2.1 Introduction 5
- 2.2 Nonmodal approach 7
  - 2.2.1 Kelvin mode approach 9
- 2.3 LAPD $\mathbf{E} \times \mathbf{B}$ flow experiment 10
- 2.4 Analytic model for sheared flow in LAPD 13
- 2.5 Simulations using nonmodal approach 19
  - 2.5.1 Drift wave initial conditions 23
- 2.6 Mode coupling and transient growth 24
- 2.7 Broadband spectrum and abrupt transitions 32
  - 2.7.1 Bypass transition and nonlinear interactions 36
  - 2.7.2 Comparison to pure vortex mode growth 36
  - 2.7.3 Effect of trapped electron instability 37
- 2.8 Comparison of nonmodal results to experimental data 38
  - 2.8.1 Recent Kevin-Helmholtz Drift-wave LAPD experiment 39
  - 2.8.2 Comparison to validated nonlinear simulation 41
- 2.9 Conclusions and discussion 43

Chapter 3. Evolution of Bounded Plasma Jet **45**
3.1 Introduction 45
3.2 Review of unbounded magnetized jets 47
3.2.1 Relation to magnetized wake field 47
3.3 Helimak configuration and parameters 48
3.4 Model equations 52
3.4.1 Boundary conditions 53
3.4.2 Rotation to field-aligned coordinates 54
3.5 Linear model equations 56
3.5.1 Chebyshev-τ solution of 3D eigenfunction 58
3.6 Spectrum, eigenfunctions and dispersion relations 59
3.7 Effects of resistive and viscous dissipation 63
3.8 Discussion 66
3.9 Future work 68

Chapter 4. Conclusions **70**
4.1 Alfvénic fluctuations in LAPD experiment 70
4.2 Evolution of bounded magnetized plasma jet in the Helimak 71

Bibliography **73**

Vita **81**

List of Tables

2.1 Parameters of the numerical simulations of equations (2.59), (2.61) and (2.62) for the LAPD shear flow experiments. 23

3.1 Helimak viscoresistive MHD parameters 69

List of Figures

2.1 A.) $\mathbf{E} \times \mathbf{B}$ measurements, and vorticity background.
B. Fluctuations of the three components of magnetic field as a function of radius [Perez, 2006]. 12

2.2 (a) Real parts of dispersive curves of the three wave modes in Eq. (2.63). The dotted line is for the drift waves. The solid line and the dashed line relate to the relatively high frequency Alfvénic-like wave modes.
(b) Imaginary part of the drift wave dispersive curve. The dispersion curves are plotted for the six dimensionless parameters $K_y = 10^3$; $V_{de} = 2 \times 10^{-3}$; $\hat{\delta}_e = 5 \times 10^{-4}$; $V_{Te}^2 = 2$; $\epsilon = 0.1$ and $S = 0$. 25

2.3 The dynamics of relations $|n_{\mathbf{k}}/\phi_{\mathbf{k}}|$ and $|\psi_{\mathbf{k}}/\phi_{\mathbf{k}}|$ for initial conditions that correspond to the pure drift wave with $K_y \ll K_x(0)$. Here $K_x(0) = 3 \times 10^4$; $K_y = 10^3$; $V_{de} = 2 \times 10^{-3}$; $\hat{\delta}_e = 5 \times 10^{-4}$; $V_{Te}^2 = 2$; $\epsilon = 0.1$ and $S = 1$ (Table I, Simulation 1). Initial conditions are defined by Eqs. (2.53)-(2.55) 27

2.4 A) The evolution of a single SFH (logarithms of real and imaginary parts of normalized fields (Ψ_1, Ψ_2, Ψ_3) are shown for the same case as in Fig. 2.2. 28

2.5 The evolution of different kinds of energies of perturbation SFH ($E_k(\tau)/E(0)$, $E_n(\tau)/E(0)$, $E_m(\tau)/E(0)$, $E(\tau)/E(0)$) for the Simulation 1 with initial conditions that correspond to a pure drift wave with $K_y \ll K_x(0)$. Here, as in Fig. 2.2, $K_x(0) = 3 \times 10^4$; $K_y = 10^3$; $V_{de} = 2 \times 10^{-3}$; $\hat{\delta}_e = 5 \times 10^{-4}$; $V_{Te}^2 = 2$; $\epsilon = 0.1$ and $S = 1$ (Simulation 1). To enlarge "the dynamically active region", the evolution is presented for times $\tau > 20$, as, initially, the growth of different energies are quite trivial: small and monotonic. 30

2.6 The red curve shows the energy associated with the plasma potential, $E_{\text{kin}}^{\perp}(\tau)$, as a fraction of the instantaneous total energy. At $\tau = 0$, the fluctuations are drift waves with plasma potential and density fluctuations of comparable magnitude. It can be seen that for a short time around $\tau \approx 30$, the magnetic energy $E_m(\tau)$ (green curve) surpasses the $E_{\text{kin}}^{\perp}(\tau)$ and the dynamics become electromagnetic. 31

2.7 The red curve shows the energy associated with the diamagnetic drift $E^{\parallel}_{\text{kin}}(\tau)$, as a fraction of the instantaneous elastic energy. When $\tau \approx 30$, the magnetic energy $E_m(\tau)$ (green curve) becomes comparable to $E^{\parallel}_{\text{kin}}(\tau)$, showing that the scales become of the order of the electron skin depth 32

2.8 Same as previous figure, but at a) $\epsilon = 0$ (Simulation 2); b) $K_x(0) = 3 \times 10^5$ and $K_y = 10^4$ (Simulation 3); c) $V^2_{Te} = 10$ (Simulation 4); d) $S = 0.3$ and $K_x(0) = 0.9 \times 10^4$ (Simulation 5). The evolution is presented for times $\tau > 10$. 33

2.9 The auto power spectrum for the plasma potential at the center of the shear region. Although turbulence is dominated by the low azimuthal modes, the frequencies extend from 5 to approximately 80 kHz. 34

2.10 Phase spectrograph for toroidal mode numbers for JET turbulence. An internal transport barrier is triggered at 6s. There is an abrupt transition from $n \approx 1$ modes to $n \approx -5$ modes. Positive n's correspond to waves with phase velocity along the current [Sharapov, 2008]. 35

2.11 The evolution of perpendicular kinetic energy of perturbation SFH $(E_k(\tau)/E(0))$ in two different cases. The dashed line relates to the considered system for the parameters presented on Fig. 2.4 c-e. The solid line relates to the pure vortex mode case (i.e., when RHS of Eq. (2.59) equal zero). The evolution is presented for times $\tau > 20$, as, initially, the growth of energies in both cases are quite identical. 37

2.12 A. The poloidal velocity profile for the 2012 LAPD experiment [Zhou, 2012]. B. The large vorticity fluctuations that are generated in the shear region versus radial location. 40

2.13 Time evolution for the power spectrum of ion saturation current fluctuations. In the 75V case (A), the spectrum begins with discrete modes. The bias has the effect of generating fluctuations of intermediate frequencies. 40

3.1 Schematic drawings of the Helimak illustrating the coordinate system used in this paper and a magnetic field line. 49

3.2 Profiles of vertical flow velocity $v_z = w(x)$ produced in the Helimak device using bias voltages A.) $V_{\text{bias}} = 0$, B.) $V_{\text{bias}} = -10$ V, and C.) $V_{\text{bias}} = -15$ V. Values are measured using Doppler shift spectroscopy of spectral atomic emission lines of singly ionized argon. 51

3.3 Langmuir probe measurements of the electric potential and the electron density in a 10eV argon plasma [Gentle, 2008]. . . . 52

3.4 The basic flow and magnetic field profiles used in the calculations in the rotated frame of reference. In the field-aligned frame of reference, rotated by an angle $\theta \approx -10.56°$, x corresponds to the radial direction; y corresponds to the the streamwise (nearly toroidal) direction; and z corresponds to the spanwise (nearly axial) direction. (Since most of our research in performed in a rotated frame of reference, we use primes to denote the laboratory frame of reference). Note that the maximum flow speed is 1/10th of the maximum Alfvén speed. 55

3.5 The complete eigenmode spectrum from Eqs. (3.8) and (3.9). They are solved for a typical axisymmetric vertical mode($\alpha = 2.3, \beta = 0.0, S = S_v = 5000$) for the reference flow profile given in Equations (3.14) - (3.17). 61

3.6 The unstable sinuous-like eigenfunction for the bounded magnetized jet ($\alpha = 2.3, \beta = 0.0, S = S_v = 5000$). For Helimak parameters, the eigenmode has an angular frequency of 2×10^5 rad/s, a growth rate of 1.4×10^4 s^{-1} and it propagates perpendicular to the helical magnetic field at $x = 0$. This eigenmode, with $k_y = \alpha/r = 4.6$ m$^{-}1$, is well into the resistive mhd regime, where $k_y \rho_s = 0.014$. 62

3.7 Dispersion relations for the two-dimensional case for different values of the spanwise wavenumber ($\beta = 0$). For these calculations $S_v = S = 5000$ and the wavenumber is normalized by the inverse of the channel half-width l. 64

3.8 Variation of growth rate with respect to spanwise wavenumber for different values of the streamwise wavenumber (α). For these calculations$S_v = S = 5000$. 65

3.9 Variation of growth rate with respect to magnetic Reynolds number (S), calculated using $\alpha = 2.3$ and $\beta = 0.0$ and a set of different values of the viscous Reynolds number (S_v). The growth rate is defined as $\omega_i = Im(L\omega/v_A)$ and $\gamma \approx 10^4$/s according to the parameters in Table I. 66

3.10 Variation of growth rate with respect to viscous Reynolds number (S_v) for different values of the magnetic Reynolds number (S). These calculations use $\alpha = 2.3$, $\beta = 0.0$, and $\omega_i = Im(L\omega/v_A)$. 67

Chapter 1

Introduction

Of the observable universe, 99.9% is in the the plasma state. Plasmas are gases of charged molecules and free electrons that exhibit all the complex density, pressure and temperature interactions of gases in addition to the often more dramatic and unexpected interactions of electromagnetic fields and the plasma. Understanding plasma phenomena is essential for the advancement of physics and many important applications, including, most notably, fusion. Plasma physics is central to the study of almost every system in space including the solar corona, solar wind and the Earth's magnetotail.

1.1 Generation of Alfvenic fluctuations in LAPD

Shear flow in laboratory and space plasmas is as ubiquitious as is the use of spectral decomposition methods to study plasma dynamics. Typically, the differential equations that describe the evolution of fluid-regime plasmas are solved by spectrally decomposing the fields into series of mutually orthonormal functions such as Fourier series. Linear systems of equations can be solved as a set of mutually orthogonal, or normal, eigenmodes. The eigenfrequencies indicate if there are any linear exponentially growing modes. Normal mode

analysis has become standard in the study of magnetohydrodynamics for many good reasons, especially its usefulness for determining the long-term stability of fields. However, it is also standard knowledge in the hydrodynamic and plasma communities that even the simplest sheared flow can make spectrally stable eigenmodes non-normal to each other. For many applications, this inconsistency has been an adequate tradeoff for the convenience provided by the normal mode analysis.

Nonetheless, it is of scientific and practical importance to understand the physics that cannot be uncovered by spectral methods. Some laboratory plasmas that are believed to be dominated by non-normality effects. In addition, non-normality effects should play a primary role in the onset of subcritical turbulence, that is, turbulence in the absence of growing linear modes. One way to probe non-normality induced physics is by solving the dynamical equations using the Kelvin Nonmodal approach. Generally, nonmodal analysis shows that strong shear flow causes eigenmodes to couple and generate transient dynamics. Examples in hydrodynamics and plasmas exist where transient dynamics couple to nonlinear mechanisms and permanently alter the system evolution, including triggering turbulence and destroying confinement in fusion experiments.

In this work, we apply the Kelvin Nonmodal method on a dynamical model and parameters that describe the plasma dynamics in the LAPD device at The University of California - Los Angeles [1]. We determine that shear flow-induced mode nonnormality can generate large transient electromagnetic,

or Alfvénic, fluctuations in the shear flow region. The results give good qualitative agreement with LAPD data presented by Perez *et al.* [2]. Most of this work is published in Horton, W., Correa, C., Chagelishvili, G., *et al.* [3].

1.2 Evolution of bounded jet

This work builds on the calculations for an unbounded magnetized plasma jet by Dahlburg *et al.* [4] by exploring how the presence of boundaries affects the dynamics of magnetized plasma jets. Magnetized jets are fluid jets superimposed on a sheared magnetic field structure. Many physical systems have a magnetized jet configuration, including solar surges and fast flows in Earth's magnetotail [5] [6] [7]. The magnetized jet is related to a magnetized wake via a Galilean transformation with respect to the maximum jet speed reference frame. For that reason, the physics of magnetized jets is also applicable to the heliospheric current sheet and and nonthermal galactic jets [8] [9]. Magnetized jets and wakes in astrophysical plasmas are effectively unbounded, but for magnetized jets in laboratory experiments, boundaries are close enough to affect the dynamics.

To model the plasma dynamics of a bounded magnetized jet, we use an analytical model consisting of three-dimensional resistive-viscous nonlinear MHD equations for a low ion temperature Argon plasma. We study the linear evolution of a magnetized jet with two no-slip boundaries. We adopt the configuration and parameters of the Helimak device at the University of Texas at Austin [10]. The Helimak device can produce a bounded magnetized jet and is

of contemporary interest because it produces magnetic field with wavelengths long enough to support Alfvén wave dynamics.

The equations are solved by expanding them as a truncated Chebyshev series and the no-slip walls are included in the form of boundary condition equations. The spectrum, eigenfunctions and dispersion relations are examined for different values of the toroidal and poloidal wavenumbers and different values of the Reynolds and Lundquist numbers. We determine which low-frequency modes arise in a bounded magnetized plasma jet configuration and how they compare to the modes of the unbounded magnetized jet; and if walls have a stabilizing effect on the modes.

This work is published in Dahlburg, R.B., Horton, W., Rowan, W.L., Correa, C., *et al.* , 2009 [11].

Chapter 2

Generation of Alfvénic fluctuations in sheared flow

2.1 Introduction

Understanding the dynamics of plasmas in the presence of strong shear flow is important to magnetically confined fusion plasma experiments. Zonal flow, which is self-organized turbulence-driven bipolar flow that locally acts like $\mathbf{E} \times \mathbf{B}$ shear flow, can reduce drift wave turbulence and reduce cross-flow transport quite universally. Zonal flow induced transport barriers have made possible record high values of confinement time and fusion output to input power ratios in tokamak plasmas, including the Joint European Torus (JET) experiment [12].

We investigate a possible explanation for the generation of a broadband spectrum of electromagnetic waves in the region with strong sheared flow of a spectrally stable plasma. Perez *et al.* [2] report Alfvénic fluctuations that appeared in a region with strong $\mathbf{E} \times \mathbf{B}$ shear flow in experiments on the Large Plasma Device (LAPD) at UCLA [1]. Similarly, Sharapov *et al.* report broad band electromagnetic waves in large zonal flow on the JET experiment [13]. The JET fluctuations were addittionally accompanied by abrupt changes in

magnetic turbulence during L-H transitions in JET palsmas. It is expected that both, the LAPD and JET observations, are related to shear flow-induced non-normality effects.

The method used here is a complement to the standard spectral treatment used to study the long-term stability of plasmas in the fluid regime. In the presence of shear flow, the typical spectral approach misses transient linear behavior that can be uncovered via the nonmodal approach. Many previous works have addresed transient dynamics that are missed by the spectral/modal approach, including Cooper, 1988 [14]. Cooper numerically describes transient linear behavior of azimuthal perturbations for flow parallel to the ambient magnetic field by means of the nonmodal approach. The LAPD phenomena studied here differ from the subject of Cooper's work in several ways, including the fact that the shear flow is perpendicular to the ambient axial field, $B_0\hat{\mathbf{e}}_z$. We apply the Kelvin Nonmodal approach to investigate whether the Alfvénic fluctuations observed in LAPD are generated by shear flow-induced non-normality.

The fluctuations that arise in zonal flow in various devices are sensitive to the device configuration and different parameter regimes within a given device [15] [16] [17] [2] [13]. Therefore, we carry out calculations for the configuration and parameters of the LAPD device.

We find good qualitative agreement between the LAPD observations and the predictions of our calculations. Our model indicates that shear flow causes spectrally stable fluctuations to become highly non-normal and, as a

result, experience linear transient growth and bursts and that the fluctuations will have a broadband spectrum. Specifically, we find that drift-wave mode turbulence couples to electromagnetic modes, generating broadband Alfvénic fluctuations. The universality of this phenomenon suggests that the same mechanism is responsible for the generation of broadband spectrum and abrupt changes in magnetic turbulence in JET.

Most of this work is presented in Horton *et al.* , 2009 [3]. In addition, ways of qualitatively comparing these numerical results to LAPD data are discussed. Recent works that attempt to relate LAPD observations to results of nonmodal calculations are reviewed [18] [19] [20] [21].

2.2 Nonmodal approach

The possibility of transient growth due to non-normality was stipulated more than a century ago[22] [23] [24]. The nonmodal method was developed by the hydrodynamic community in the 1990s to address the non-normality of spectrally stable nonuniform flows [25]. It was shown that spectrally stable flows can experience significant transient growth and that positive feedback mechanisms involving nonlinear interactions can create a positive feedback mechanism that leads to the transition to turbulence. This development has not been extensively applied to study plasma phenomena [26] [27] but there is growing recognition of the role of non-normality effects in the onset of turbulence, especially in spectrally stable plasmas.

The spectral/modal method of studying the stability of flow dynamics

is to turn the initial value problem into an eignevalue problem by assuming a normal mode ansatz, that is, one with an exponential time dependence. For an example involving Fourier spectral expansion of the spatial directions, the normal mode ansatz can be

$$\exp\left(i(k_x x + k_y y - \omega t\right) \ . \tag{2.1}$$

The N wavenumbers k_x and k_y are assumed to be constant and any imaginary part of the eigenvalues gives the exponential growth rate of the corresponding eigen mode. Applying this ansatz to the dynamical equations of the system, followed by linearizing, produces the set of linear normal operators that describe the system. The eigenmodes are assumed to be normal to each other, or linearly independent of each other. The spectral approach makes solving the set of differential evolution equations vastly easier than solving the initial value problem and it has led to a focus on the asymptotic stability of flows.

An exponentially growing solution in hydrodynamic flow (a linear spectral instability) can only occur if the equilibrium velocity profile has an inflection point [28]. Therefore, all shear flows without an inflection point are spectrally stable. Yet, several laboratory experiments and numerical simulations show that perturbations in spectrally stable smooth shear flows may cause a transition from a laminar to a turbulent state [25].

In the presence of highly sheared flows, the linear operators related to fluctuations of the plasma become strongly non-normal . A consequence is that the eigenmodes of the system are not linearly independent and, therefore, gen-

erally interfere. For a normal linear system, a superposition of spectrally stable or even spectrally decaying, non-normal modes will eventually decay, but even spectrally decaying modes that become non-normal can produce growth for finite times. Spectral analysis of non-normal systems misses these finite time period dynamics; which are usually speculated to be insignificant.

2.2.1 Kelvin mode approach

Several works have presented alternatives to the spectral approach to describe non-normality induced finite-time dynamics in fluids in a variety of shear flows [29] [30] [31] [32]. This work uses the Kelvin Nonmodal approach [22], which has been used widely to describe constant shear flow and informs smooth shear flow phenomena [33] [34] [35] [36] [37] [38] [39] [40] [41] [42] [43].

The Kelvin Nonmodal approach uses Kelvin modes, which are a type of ansatz with a time-dependent phase due to the usual frequency as well as due to wavenumbers that are time-dependent. Kelvin modes can be thought of as "flowing eigenfunctions" in expanding fluctuations. For a shear flow $v_y(x) = Sx$, a Fourier Kelvin mode would be

$$\exp\left(i(k_x(\tau)x + k_y y - \omega\tau\right) \ , \tag{2.2}$$

with $k_x(\tau) = k_x(0) - Sk_y\tau$. This formulation is well established and has been used extensively since the 1990s [33] [34] [35] [36] [37] [38] [39] [40] [42] [41] [43]. Kelvin modes are valid for systems with linear shear flow, and can produce approximate solutions for systems with more complicated shear flow. To

account for the fact that the flow varies spatially ($v_y(x) = Sx$), the convective derivative must be modified to include the contribution due to the sheared part of the flow,

$$\frac{\partial}{\partial t} = \frac{\partial}{\partial t} + v_y(x)\frac{\partial}{\partial y} \tag{2.3}$$

The Kelvin Nonmodal approach yields a description of the transient exchange of energy between shear flow and perturbations. Landahl *et al.* explain how shear flow non-normality induces transient growth of vortical perturbations by means of conservation laws [44]. An alternate explanation, that uses dynamical equations to solve the dynamics of a fluid parcel, is presented by Chagelishvili [45].

2.3 LAPD $\mathbf{E} \times \mathbf{B}$ flow experiment

The cylindrical plasma column produced in the LAPD experiments is 18m long and 0.6 m in diameter; the device has a 1m diameter. The singly-ionized Helium plasma is created by a 20ms long pulsed discharge from a Barium Oxide coated emmissive cathode. Coils along the length of the chamber produce an ambient field that is uniform radially and nearly uniform axially ($\partial_z B_z / B_0 < 5\%$). The chamber wall is biased with respect to the anode and cathode for 5ms, establishing a variety of electric field profiles with a radial component, depending on the bias voltage and the magnetic field boundary conditions. The chosen electric field profile for this experiment produces a strong electric field that acts with the axial ambient magnetic field to produce a radially inward sheared $\mathbf{E} \times \mathbf{B}$ flow that is nearly linear with radius.

Measurements of magnetic field and plasma density, temperature, and floating potential are taken with a three-component magnetic probe, a vorticity probe, and a mach probe.

The reported maximum $\mathbf{E} \times \mathbf{B}$ flow is $U_E \approx 4 \times 10^5$ cm/s at the center of the shear flow region; the radial width of the shear flow region is $L_E \approx 5$cm; and the Alfvén speed $v_A \approx 9 \times 10^7$ cm/s. The density gradient has a scale length $L_n = -n/(dn/dx)$ of about 5 cm, comparable to the flow scale length L_E. The electron temperature rises slightly at the column edge but it is otherwise uniform.

The flow shear can be characterized by $A = U_E/L_E \approx 10^5 s^{-1}$. For characterisitc flow speed v_A and characteristic axial length $L_{||} \approx 10^3$cm, the normalized shear is $S = AL_{||}/v_A \approx 0.9$. The eigenmodes associated with the flow are highly non-normal when $S \approx 1$.

These LAPD experiments with $\mathbf{E} \times \mathbf{B}$ flow driven turbulence revealed the generation of Alfvénic-like, or electromagnetic, fluctuations in a region of strong flow shear [2]. The observed fluctuations of the radial component of the magnetic field had a high frequency broadband spectrum. Although they were small, of order $\delta B/B_0 \approx 10^{-5}$, the relative increase in amplitude in the region of shear was significant. The generation of electromagnetic fluctuations is important because they can modify the anomalous transport.

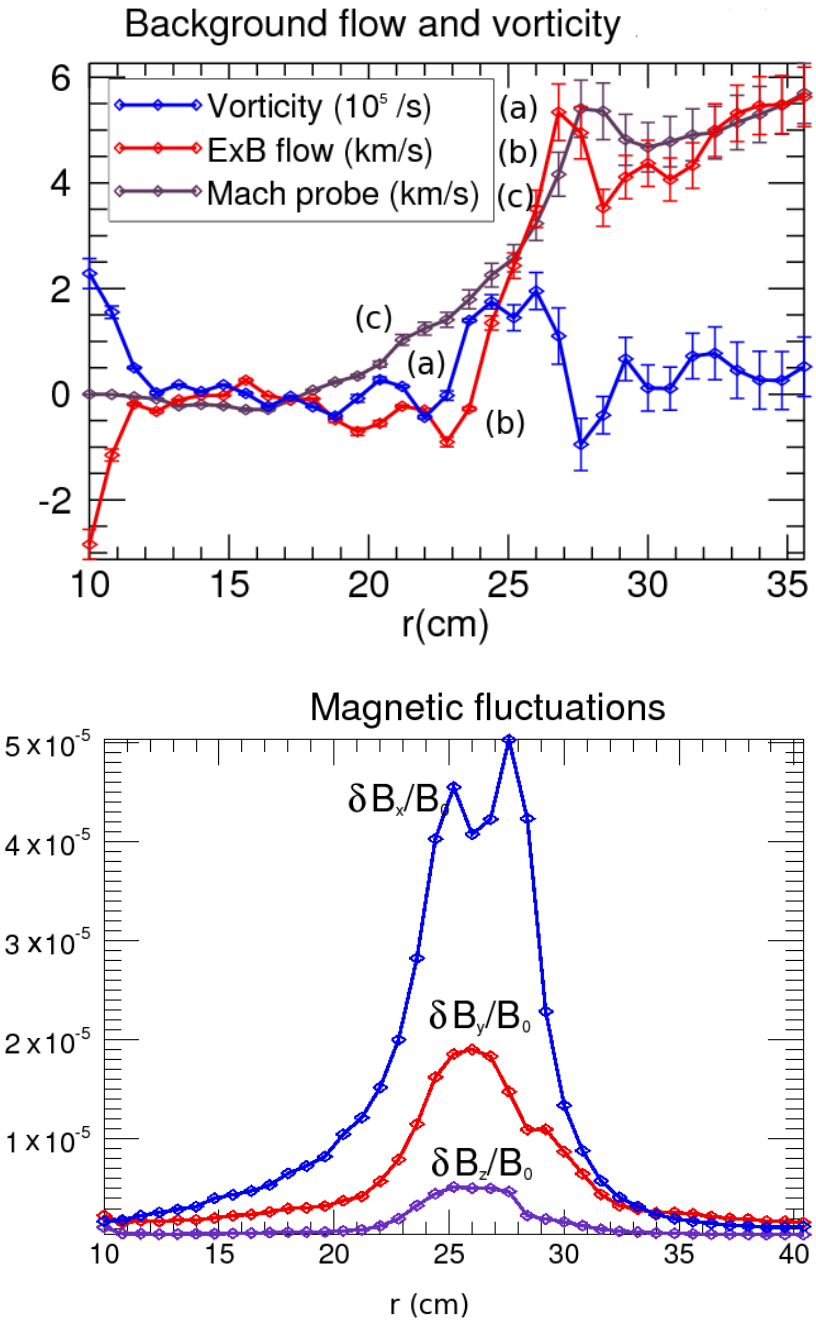

Figure 2.1: A.) $\mathbf{E} \times \mathbf{B}$ measurements, and vorticity background.
B. Fluctuations of the three components of magnetic field as a function of radius [Perez, 2006].

2.4 Analytic model for sheared flow in LAPD

In this section, we derive the reduced plasma equations for the conditions of the LAPD experiment. The uniform background magnetic field direction is taken as the z-direction. The zonal flow region width is about 1/6th of the plasma column radius, and therefore we employ a local Cartesian frame with the radial direction taken as the x-direction. The poloidal direction is taken to be straight and is represented by the y-direction.

The three model equations are written for perturbations of the scalar electrostatic potential $\tilde{\phi}$; the component of the electromagnetic vector potential parallel to the mean magnetic field $A_z = -\tilde{\psi}$; and the density $\tilde{n}$. The equations are based on a two-fluid MHD model.

The electrostatic and magnetic potentials are represented by $\phi = \phi_0(x) + \tilde{\phi}$ and $\tilde{\psi}$, and the electric and magnetic fields are

$$\mathbf{E}_\perp = -\nabla_\perp \phi \ , \tag{2.4}$$

$$E_{||} = -\hat{\mathbf{b}} \cdot \nabla \phi + \frac{1}{c} \frac{\partial \tilde{\psi}}{\partial t} \ , \tag{2.5}$$

$$\mathbf{B} = B_0 \mathbf{e}_z + \delta \mathbf{B} = B_0 \mathbf{e}_z + \mathbf{e}_z \times \nabla_\perp \tilde{\psi} \ , \tag{2.6}$$

where $\phi_0(x)$ is the mean electrostatic potential and B_0 is the value of the background magnetic field.

The cross-field electron and ion drift velocities have the form

$$\mathbf{v}_{e\perp} = \mathbf{v}_E + \mathbf{v}_{de} \ , \quad \mathbf{v}_{i\perp} = \mathbf{v}_E + \mathbf{v}_{pi} \ , \tag{2.7}$$

where $\mathbf{v}_E$ and $\mathbf{v}_{0y}$ are the full and mean sheared $\mathbf{E}\times\mathbf{B}$ flow velocities

$$\mathbf{v}_E = c\frac{\mathbf{E}_\perp\times\mathbf{B}}{B_0^2} = \frac{c}{B_0}(\mathbf{e}_z\times\nabla_\perp\phi)\ , \tag{2.8}$$

$$\mathbf{v}_{0y} = \frac{c}{B_0}(\mathbf{e}_z\times\nabla_\perp\phi_0) = \frac{c}{B_0}\frac{\partial\phi_0}{\partial x}\mathbf{e}_y\ , \tag{2.9}$$

$\mathbf{v}_{de}$ and $\mathbf{v}_{pi}$ are electron diamagnetic drift and ion polarization drift velocities

$$\mathbf{v}_{de} = -c\frac{\hat{\mathbf{b}}\times\nabla p_e}{en_0B_0} = -\frac{ck_BT_e}{eB_0}\frac{1}{n_0}\frac{\partial n_0}{\partial x}\mathbf{e}_y\ , \tag{2.10}$$

$$\mathbf{v}_{pi} = \frac{c}{\omega_{ci}B_0}\frac{dE_\perp}{dt} = -\frac{m_ic^2}{eB_0^2}\frac{d}{dt}\nabla_\perp\phi\ , \tag{2.11}$$

$n = n_0(x)+\tilde{n}$, p_e and T_e are the electron density, pressure and temperature, and L_n is the zonal flow radial size. The basic zonal flow velocity $\mathbf{v}_{0y}$ is directed along the y-axis and defines the convective time derivative:

$$\frac{d}{dt} = \frac{\partial}{\partial t} + \mathbf{v}_{0y}\cdot\nabla\ . \tag{2.12}$$

In Alfvén-Drift wave turbulence, there are two important nonlinear directional derivatives given by

$$\delta\mathbf{B}\cdot\boldsymbol{\nabla}f = \frac{1}{B_0}(\mathbf{e}_z\times\nabla_\perp\tilde{\psi})\cdot\nabla f = \frac{1}{B_0}\left[\psi,f\right] \tag{2.13}$$

$$\begin{aligned}\mathbf{v}_E\cdot\boldsymbol{\nabla}f &= \frac{c}{B_0}\frac{\partial\phi_0}{\partial x}\mathbf{e}_y + \frac{c}{B_0}(\mathbf{e}_z\times\nabla_\perp\tilde{\phi}\\ &= v_{0y}\partial_y f\mathbf{e}_y + \frac{c}{B_0}\left[\psi,f\right]\ .\end{aligned} \tag{2.14}$$

These poisson bracket nonlinear terms are directional derivatives are Lie derivatives along the dynamical vector fields. Lie derivatives are strongly nonlinear when the fluctuation amplitudes reach the levels $\delta B/B_0 = |\mathbf{k}_\parallel|/k_\perp$ and

$v_E = |\omega|/k_\perp$. In nonlinear vortices, both nonlinearities reach their limiting values, which are largest for the lowest values of $k_\perp$.

The first equation, for $\tilde{\phi}$, is derived from the charge conservation equation $\partial(q_i n_i - q_e n_e)/\partial t + \nabla \cdot (q_i n_i \mathbf{v}_i - q_e n_e \mathbf{v}_e) = 0$. For a quasi-neutral incompressible fluid,

$$\nabla \cdot (en(\mathbf{v}_i - \mathbf{v}_e)) = 0 \tag{2.15}$$

$$\nabla_\perp \cdot \mathbf{J}_\perp = -\nabla_{||} J_{||} \ . \tag{2.16}$$

Equation (2.16) is valid once the plasma density is sufficiently high. Taking into account the axial component of Ampere's law ($\nabla_\perp^2 \tilde{\psi} = 4\pi J_{||}/c$) and the parallel electron current expression ($J_{||} = -env_{||}$), one can express the parallel electron velocity via $\tilde{\psi}$

$$v_{||} = -\frac{c}{4\pi en} \nabla_\perp^2 \tilde{\psi} \ . \tag{2.17}$$

The perpendicular current is supplied by the ion polarization drift:

$$\mathbf{J}_\perp = en\mathbf{v}_{pi} = -\frac{nm_i c^2}{B^2} \left(\frac{\partial}{\partial t} + v_{0y} \frac{\partial}{\partial y} \right) \nabla_\perp \phi \ . \tag{2.18}$$

Substituting expressions of $\mathbf{J}_\perp$ and $J_{||}$ from Eqs. (2.17), and (2.18) into Eq. (2.16), we obtain

$$\left(\frac{\partial}{\partial t} + v_{0y} \frac{\partial}{\partial y} \right) \nabla_\perp^2 \tilde{\phi} - \frac{\partial^2 v_{0y}}{\partial x^2} \frac{\partial \tilde{\phi}}{\partial y} = \frac{V_A^2}{c} \frac{\partial}{\partial z} (\nabla_\perp^2 \tilde{\psi}), \tag{2.19}$$

where $v_A = B_0/\sqrt{4\pi m_i n_0}$ is the Alfvén velocity.

The second field equation, for $\widetilde{n}$, is derived from the electron continuity equation

$$\frac{\partial n_e}{\partial t} + \nabla(n_e \mathbf{v_e}) = 0 \ , \tag{2.20}$$

or

$$\frac{\partial \tilde{n}_e}{\partial t} + \mathbf{v}_e \cdot \nabla(n_0(x) + \tilde{n}) = -(n_0(x) + \tilde{n})(\nabla \cdot \mathbf{v}_e) \ . \tag{2.21}$$

Taking into account Eqs. (2.7)-(2.10), and (2.17), in the linear regime, the second term of the LHS of Eq. (2.21) and the RHS of Eq.(2.21) become

$$\mathbf{v}_e \cdot \nabla(n_0(x) + \tilde{n}) = v_{0y} \frac{\partial \tilde{n}}{\partial y} - \frac{c}{B} \frac{\partial \tilde{\psi}}{\partial z} \frac{\partial n_0(x)}{\partial x} \ , \tag{2.22}$$

and

$$-(n_0(x) + \tilde{n})(\nabla \cdot \mathbf{v}_e) = -n_0(x) \frac{\partial v_{||}}{\partial z} = \frac{c}{4\pi e} \frac{\partial}{\partial z} \nabla_\perp^2 \tilde{\psi} \ . \tag{2.23}$$

Introducing the density inhomogeneity scale length $L_n = -n/(\partial n_0(x)/\partial x)$, finally, the second equation reduces to

$$\left(\frac{\partial}{\partial t} + v_{0y} \frac{\partial}{\partial y} \right) \frac{\tilde{n}_e}{n_0} + \frac{c}{B L_n} \frac{\partial \tilde{\phi}}{\partial y} = \frac{c}{4\pi e n_0} \frac{\partial}{\partial z} \nabla_\perp^2 \tilde{\psi} \ . \tag{2.24}$$

The third equation, for $\tilde{\psi}$, is derived from the linearized electron parallel momentum equation, as the parallel electric field $E_{||}$ accelerates the electrons in the absence of significant resistivity according to

$$m_e n_0 \left(\frac{\partial}{\partial t} + v_{0y} \frac{\partial}{\partial y} \right) v_{||e} = -enE_{||} - \nabla_{||} p_e \, . \tag{2.25}$$

From Eqs. (2.4), and (2.13) in the linear limit follows:

$$E_{||} = -\frac{\partial \tilde{\phi}}{\partial z} - \frac{1}{B_0} \frac{\partial \tilde{\psi}}{\partial y} + \frac{1}{c} \frac{\partial \tilde{\psi}}{\partial t} = -\frac{\partial \tilde{\phi}}{\partial z} + \frac{1}{c} \left(\frac{\partial}{\partial t} + v_{0y} \frac{\partial}{\partial y} \right) \tilde{\psi} \ , \tag{2.26}$$

$$\nabla_{||} p_e = k_B T_e \nabla_{||} n = k_B T_e \left(\frac{\partial \tilde{n}}{\partial z} - \frac{1}{B_0} \frac{\partial n_0}{\partial x} \frac{\partial \tilde{\psi}}{\partial y} \right) = n_0 \left(k_B T_e \frac{\partial}{\partial z} \frac{\tilde{n}}{n_0} + \frac{e v_{de}}{c} \frac{\partial \tilde{\psi}}{\partial y} \right) \tag{2.27}$$

Taking into account Eqs. (2.17), (2.26), (2.27), and Eq.(2.25) becomes:

$$(1-\delta_e^2\nabla_\perp^2)\left(\frac{\partial}{\partial t}+v_{0y}\frac{\partial}{\partial y}\right)\tilde{\psi}=c\frac{\partial}{\partial z}\left(\tilde{\phi}-\frac{k_BT_e}{e}\frac{\tilde{n}}{n_0}\right)-v_{de}\frac{\partial\tilde{\psi}}{\partial y}\ , \tag{2.28}$$

where $\delta_e^2\equiv c^2/\omega_{pe}^2$. This model neglects the small fluctuations in the electron temperature.

In summary, the sytem of linear equations is

$$\frac{d}{dt}(\nabla_\perp^2\tilde{\phi})-\frac{\partial^2 v_{0y}(x)}{\partial x^2}\frac{\partial\tilde{\phi}}{\partial y}=\frac{V_A^2}{c}\frac{\partial}{\partial z}(\nabla_\perp^2\tilde{\psi}), \tag{2.29}$$

$$\frac{k_BT_e}{e}\frac{d}{dt}\left(\frac{\tilde{n}}{n_0}\right)+v_{de}\frac{\partial\tilde{\phi}}{\partial y}=\frac{v_{Te}^2\delta_e^2}{c}\frac{\partial}{\partial z}\left(\nabla_\perp^2\tilde{\psi}\right), \tag{2.30}$$

$$\frac{d}{dt}\left[\left(1-\delta_e^2\nabla_\perp^2\right)\tilde{\psi}\right]=c\frac{\partial}{\partial z}\left(\tilde{\phi}-\frac{k_BT_e}{e}\frac{\tilde{n}}{n_0}\right)-v_{de}\frac{\partial\tilde{\psi}}{\partial y}, \tag{2.31}$$

where $\tilde{\phi}$, $-\tilde{\psi}$ and $\tilde{n}$ are perturbations of the scalar electrostatic potential, the axial vector potential and the density, respectively. The corresponding zonal flow velocity, magnetic field and density are

$$\mathbf{v}_e=\frac{c}{B}(\mathbf{e}_z\times\nabla_\perp\phi)=v_{0y}(x)\mathbf{e}_y+\frac{c}{B}(\mathbf{e}_z\times\nabla_\perp\tilde{\phi}); \tag{2.32}$$

$$\mathbf{B}=B_0\mathbf{e}_z+\mathbf{e}_z\times\nabla\tilde{\psi}; \tag{2.33}$$

$$n=n_0(x)+\tilde{n}; \tag{2.34}$$

The other quantities used are the electron temperature and charge, T_e and e; the electron drift velocity, $v_{de}\equiv ck_BT_e/eB_0L_n=C_s\rho_s/L_n$; the Alfvén velocity, $V_A=(B_0^2/4\pi m_in_0)^{(1/2)}$; the electron thermal velocity, $v_{Te}=$

$\sqrt{k_B T_e/m_e}$; the ion sound velocity, $C_s = \sqrt{k_B T_e/m_i}$; the density inhomogeneity scale length (the zonal flow radial size), L_n; the ion inertial scale length, $\rho_s = C_s/\omega_{ci}$; and the electron inertial length, $\delta_e \equiv c/\omega_{pe}$.

Switching to length and time scales normalized by the axial length scale $1/k_{||}$ and the Alfvén time $1/(k_{||}v_A)$, the normalized physical quantities are

$$(x,y,z)k_{||} = (X,Y,Z), \quad tk_{||}V_A = \tau, \quad \frac{A}{k_{||}V_A} = S,$$
$$\frac{v_{de}}{V_A} = V_{de}, \quad \frac{v_{Te}}{V_A} = V_{Te}, \quad \rho_s^2 k_{||}^2 = \hat{\rho}_s^2, \quad \delta_e^2 k_{||}^2 = \hat{\delta}_e^2,$$

$$\begin{pmatrix} \frac{C_s}{V_A}\frac{e}{k_B T_e}\tilde{\phi} \\ \frac{C_s}{V_A}\frac{\tilde{n}}{n_0} \\ \frac{C_s}{c}\frac{e}{k_B T_e}\tilde{\psi} \end{pmatrix} = \begin{pmatrix} \hat{\phi} \\ \hat{n} \\ \hat{\psi} \end{pmatrix}. \tag{2.35}$$

$$\frac{d}{dt}(\nabla_\perp^2\tilde{\phi}) - \frac{\partial^2 v_{0y}(x)}{\partial x^2}\frac{\partial\tilde{\phi}}{\partial y} = \frac{V_A^2}{c}\frac{\partial}{\partial z}(\nabla_\perp^2\tilde{\psi}), \tag{2.36}$$

$$\frac{k_B T_e}{e}\frac{d}{dt}\left(\frac{\tilde{n}}{n_0}\right) + v_{de}\frac{\partial\tilde{\phi}}{\partial y} = \frac{v_{Te}^2\delta_e^2}{c}\frac{\partial}{\partial z}\left(\nabla_\perp^2\tilde{\psi}\right), \tag{2.37}$$

$$\frac{d}{dt}\left[\left(1-\delta_e^2\nabla_\perp^2\right)\tilde{\psi}\right] = c\frac{\partial}{\partial z}\left(\tilde{\phi} - \frac{k_B T_e}{e}\frac{\tilde{n}}{n_0}\right) - v_{de}\frac{\partial\tilde{\psi}}{\partial y}, \tag{2.38}$$

As stated before, the Kelvin approach involves expanding the model equations according to the convective derivative

$$\frac{d}{dt} \equiv \frac{\partial}{\partial t} + v_{0y}(x)\frac{\partial}{\partial y}; \tag{2.39}$$

The linear spatial fourier harmonic operators (SFHs) acquire a time dependence given by

$$K_x(\tau) = K_x(0) - SK_y\tau\ , \tag{2.40}$$

where $S = dv_y/dx$ is the flow shear normalized by the Alfvén time $k_{||}V_A$. The wave numbers of the SFHs (Kelvin modes) vary in time along the flow shear. In the linear approximation, SFHs "drift" in the **K**-space (in wavenumber space).

In this notation, Eqs. (2.36)-(2.38)reduced to:

$$\left(\frac{\partial}{\partial\tau} + SX\frac{\partial}{\partial Y}\right)(\nabla_\perp^2\hat{\phi}) = \frac{\partial}{\partial Z}(\nabla_\perp^2\hat{\psi}), \tag{2.41}$$

$$\left(\frac{\partial}{\partial\tau} + SX\frac{\partial}{\partial Y}\right)\hat{n} + V_{de}\frac{\partial\hat{\phi}}{\partial Y} = V_{Te}^2\hat{\delta}_e^2\frac{\partial}{\partial Z}\left(\nabla_\perp^2\hat{\psi}\right), \tag{2.42}$$

$$\left(\frac{\partial}{\partial\tau} + SX\frac{\partial}{\partial Y}\right)\left[\left(1-\hat{\delta}_e^2\nabla_\perp^2\right)\hat{\psi}\right] = \frac{\partial\hat{\phi}}{\partial Z} - \frac{\partial\hat{n}}{\partial Z} - V_{de}\frac{\partial\hat{\psi}}{\partial Y}, \tag{2.43}$$

2.5 Simulations using nonmodal approach

Consider a SFH for which $K_x(0)/K_y \gg 1$ and, thus, the action of the shear S is negligible. In this case, the trapped-particle instability term ($\epsilon \simeq 0$) can be neglected. Assuming

$$\begin{pmatrix} \phi_{\mathbf{k}}(\tau) \\ n_{\mathbf{k}}(\tau) \\ \psi_{\mathbf{k}}(\tau) \end{pmatrix} = \begin{pmatrix} \phi_{\mathbf{k}} \\ n_{\mathbf{k}} \\ \psi_{\mathbf{k}} \end{pmatrix} \exp\left(-i\omega_\Re\tau\right) \ , \tag{2.44}$$

Eqs. (2.59)-(2.61) become:

$$-\,\omega_\Re\left(K_x(0), K_y\right)\phi_{\mathbf{k}} = \psi_{\mathbf{k}}, \tag{2.45}$$

$$-\ \omega_\Re\left(K_x(0), K_y\right)n_{\mathbf{k}} \ + \ K_y V_{de}\phi_{\mathbf{k}} \quad = \quad -V_{Te}^2\hat{\delta}_e^2\left(K_x^2(0) + K_y^2\right)\psi_{\mathbf{k}}, \tag{2.46}$$

$$-\left[1+\hat{\delta}_e^2\left(K_x^2(0)+K_y^2\right)\right]\omega_{\Re}\left(K_x(0),K_y\right)\psi_{\mathbf{k}} = \phi_{\mathbf{k}} - n_{\mathbf{k}} - K_y V_{de}\psi_{\mathbf{k}}. \quad (2.47)$$

In terms of $\phi_{\mathbf{k}}$, the plasma density $n_{\mathbf{k}}$ and poloidal flux function $\psi_{\mathbf{k}}$ are

$$n_{\mathbf{k}} = \left[\frac{K_y V_{de}}{\omega_{\Re}\left(K_x(0),K_y\right)} - V_{Te}^2\hat{\delta}_e^2\left(K_x^2(0)+K_y^2\right)\right]\phi_{\mathbf{k}}, \quad (2.48)$$

$$\psi_{\mathbf{k}} = -\omega_{\Re}\left(K_x(0),K_y\right)\phi_{\mathbf{k}}. \quad (2.49)$$

Solving the dispersion Eq.(2.63) at $K_x = K_x(0)$ and defining the drift wave frequency (i.e. the smallest $|\omega_{\Re}|$) as $\omega_{\Re}(K_x(0),K_y) \equiv \omega_0$, Eqs. (2.48) and (2.49) take the form:

$$n_{\mathbf{k}} = \left[\frac{K_y V_{de}}{\omega_0} - V_{Te}^2\hat{\delta}_e^2\left(K_x^2(0)+K_y^2\right)\right]\phi_{\mathbf{k}}, \quad (2.50)$$

$$\psi_{\mathbf{k}} = -\omega_0\phi_{\mathbf{k}}. \quad (2.51)$$

At $K_x(0)/K_y \gg 1$, $\omega_0 \ll 1$ and, consequently, $\psi_{\mathbf{k}} \ll \phi_{\mathbf{k}}$. Finally, separating the fields into the real and imaginary parts according to

$$\phi_{\mathbf{k}} = \phi'_{\mathbf{k}} + \mathrm{i}\phi''_{\mathbf{k}}, \quad n_{\mathbf{k}} = n'_{\mathbf{k}} + \mathrm{i}n''_{\mathbf{k}}, \quad \psi_{\mathbf{k}} = \psi'_{\mathbf{k}} + \mathrm{i}\psi''_{\mathbf{k}}, \quad (2.52)$$

one can write initial conditions for numerical solutions of Eqs. (2.64)-(2.69) as:

$$\phi''_{\mathbf{k}} = 0; \qquad \phi'_{\mathbf{k}} = 1; \quad (2.53)$$

$$n''_{\mathbf{k}} = 0; \qquad n'_{\mathbf{k}} = \frac{K_y V_{de}}{\omega_0} - V_{Te}^2\hat{\delta}_e^2\left(K_x^2(0)+K_y^2\right); \quad (2.54)$$

$$\psi''_{\mathbf{k}} = 0; \qquad \psi'_{\mathbf{k}} = -\omega_0. \quad (2.55)$$

The zonal flow profile is approximately piece-wise linear, $v_y = Ax$ with a shear rate $A \approx 0.8 \times^5 \ s^{-1}$ in the sheared region. Expanding the convective derivative, normalizing, and adopting a linear v_y, Eqs. (2.29) - (2.31) reduce to

$$\left(\frac{\partial}{\partial\tau} + SX\frac{\partial}{\partial Y}\right)(\nabla_\perp^2\hat{\phi}) = \frac{\partial}{\partial Z}(\nabla_\perp^2\hat{\psi}), \tag{2.56}$$

$$\left(\frac{\partial}{\partial\tau} + SX\frac{\partial}{\partial Y}\right)\hat{n} + V_{de}\frac{\partial\hat{\phi}}{\partial Y} = V_{Te}^2\hat{\delta}_e^2\frac{\partial}{\partial Z}\left(\nabla_\perp^2\hat{\psi}\right), \tag{2.57}$$

$$\left(\frac{\partial}{\partial\tau} + SX\frac{\partial}{\partial Y}\right)\left[\left(1-\hat{\delta}_e^2\nabla_\perp^2\right)\hat{\psi}\right] = \frac{\partial\hat{\phi}}{\partial Z} - \frac{\partial\hat{n}}{\partial Z} - V_{de}\frac{\partial\hat{\psi}}{\partial Y}, \tag{2.58}$$

Using the time-dependent operators introduced in Eq. (2.40), the model equations become

$$K_\perp^2(\tau)\frac{\partial\phi_{\mathbf{k}}}{\partial\tau} - 2SK_x(\tau)K_y\phi_{\mathbf{k}} = \mathrm{i}K_\perp^2(\tau)\psi_{\mathbf{k}}, \tag{2.59}$$

$$\frac{\partial n_{\mathbf{k}}}{\partial\tau} + \mathrm{i}K_yV_{de}(1+\mathrm{i}\epsilon)\phi_{\mathbf{k}} = -\mathrm{i}V_{Te}^2\hat{\delta}_e^2K_\perp^2(\tau)\psi_{\mathbf{k}}, \tag{2.60}$$

and

$$\left[1+\hat{\delta}_e^2K_\perp^2(\tau)\right]\frac{\partial\psi_{\mathbf{k}}}{\partial\tau} - 2S\hat{\delta}_e^2K_x(\tau)K_y\psi_{\mathbf{k}} = \mathrm{i}\phi_{\mathbf{k}} - \mathrm{i}n_{\mathbf{k}} - \mathrm{i}K_yV_{de}\psi_{\mathbf{k}}, \tag{2.61}$$

where $K_\perp^2(\tau) \equiv K_x^2(\tau) + K_y^2$ and Eq. (2.59) is modified to include a term leading to the trapped-particle instability [46]. We keep this term even though the trapped particle instability is negligibly slow ($\epsilon << 1$) compared to drift wave dynamics and the transient growth being studied, in order to test how the transient growth varies with different values of ϵ.

In the shearless limit ($S = 0$) Eq. (2.59) gives that when the axial vector potential is comparable to the electrostatic potential (when $\|K_x/K_y\| \leq 1$ and $\omega_{Re} \approx 1$), drift waves have a small electromagnetic component due to the parallel plasma current produced by $en_eE_{||} \approx -k_BT_e\nabla_{||}n_e$. In contrast, as $\|K_x/K_y\| \to 0$, drift waves become electrostatic. The other two modes, which are Alfvénic-like with high frequency ($(1/k_{||}V_A)\|\omega_{Re} > 1$), have dominant magnetic fluctuations ofr all K_x. Sufficiently strong and localized zonal flows create a plasma version of the Kelvin-Helmholtz instability.

The time-dependence of the wavenumber vector $\mathbf{K}(\tau)$ is induced by the shear flow parameter S. Its effect is to stretch the initial ϕ, n, and ψ structures in the direction of the sheared flow as they are convected by the flow. This result coincides with the measurement by Carter and Maggs, 2009 showing that the two-dimensional correlation function is stretched in the direction of the sheared flow in direct proportion to the electric field bias level [47].

This system of equations corresponds to spectrally stable drift waves. In fact, in accordance to [46], low frequency drift waves are subject to the trapped-particle instability. To account for such instability, Eq. (2.60) becomes:

$$\frac{\partial n_{\mathbf{k}}}{\partial \tau} + \mathrm{i}K_yV_{de}(1 + \mathrm{i}\epsilon)\phi_{\mathbf{k}} = -\mathrm{i}V_{Te}^2\hat{\delta}_e^2K_\perp^2(\tau)\psi_{\mathbf{k}}, \tag{2.62}$$

where the trapped particle contribution $\epsilon \ll 1$.

Five simulations are done for the parameter sets in Table 2.1 to test the sensitivity of the results to different effects. Simulation 1 best matches the

Table 2.1: Parameters of the numerical simulations of equations (2.59), (2.61) and (2.62) for the LAPD shear flow experiments.

Sim.	K_y	$K_x(0)$	V_{de}	$\hat{\delta}_e$	V_{Te}^2	ϵ	S
1	10^3	3×10^4	2×10^{-3}	5×10^{-4}	2	0.1	1
2	10^3	3×10^4	2×10^{-3}	5×10^{-4}	2	0	1
3	10^4	3×10^5	2×10^{-3}	5×10^{-4}	2	0.1	1
4	10^3	3×10^4	2×10^{-3}	5×10^{-4}	10	0.1	1
5	10^3	0.9×10^4	2×10^{-3}	5×10^{-4}	2	0.1	0.3

parameters of the LAPD experiment and it is therefore used as the baseline case.

2.5.1 Drift wave initial conditions

For the appropriate initial values, these equations describe the dynamics of a perturbaton SFH as an initial valua problem. The dynamics depend on which mode, or mixture of modes, the system is initialized with.

We initialize the system with an SFH nearly corresponding to a drift wave perturbation with $K_x(0)/K_y >> 1$. Eqs. (2.64)-(2.69) are solved using the Mathematica numerical ODE solver, which is an implementation of the non-stiff Adams method and a stiff Gear backward differentiation method. To write the initial conditions for the pure drift wave SFH, we use the fact that the dynamics of drift wave SFHs is only negligibly affected by the action of the flow shear.

The dispersion in the shearless limit ($S = 0$) describes the basic spectrum of our model. Fourier-expanding the linear equations with constant

wavelength harmonics and an exponential time dependence $\exp(-i\omega\tau)$ gives

$$\omega^3\left(1+\hat{\delta}_e^2\left(K_x^2+K_y^2\right)\right)-\omega^2 K_y V_{de} \\ -\omega\left(1+V_{Te}^2\hat{\delta}_e^2\left(K_x^2+K_y^2\right)\right)+(1+\mathrm{i}\epsilon)K_y V_{de}=0. \quad (2.63)$$

In uniform flow, there are two high frequency kinetic Alfvén waves and a low frequency drift wave. The Alfvénic-like fluctuations are dispersive with ω dependent on K_x. Since shear gives K_x a time dependence, the frequency ω also acquires a time dependence.

The real and imaginary parts of (2.63) for the parameters in Table 2.1 are plotted for a different values of K_x in Fig. 2.8. Note that simulation 5 uses $K_x(0) = 0.9 \times 10^4$ to produce the same dynamical time $\tau_{\mathrm{dyn}} = K_x(0)/K_y S$ as in the previous simulations.

The plots in Fig. 2.2 show that for all values that K_x may take, the frequencies of the Alfvénic-like fluctuation branches are substantially different from the drift wave frequencies. Therefore, the coupling between the drift and Alfvénic-like fluctuations is exclusively nonresonant.

2.6 Mode coupling and transient growth

In addition to describing the energy exchange between shear flow and perturbations, the Kelvin approach also exposes two channels of *linear coupling* of perturbation modes. The first channel of energy exchange is between

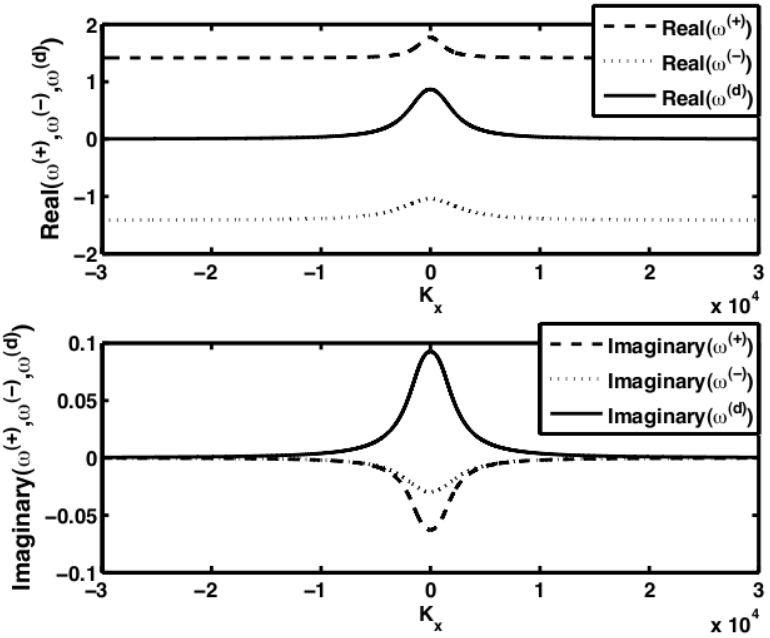

Figure 2.2: (a) Real parts of dispersive curves of the three wave modes in Eq. (2.63). The dotted line is for the drift waves. The solid line and the dashed line relate to the relatively high frequency Alfvénic-like wave modes. (b) Imaginary part of the drift wave dispersive curve. The dispersion curves are plotted for the six dimensionless parameters $K_y = 10^3$; $V_{de} = 2 \times 10^{-3}$; $\hat{\delta}_e = 5 \times 10^{-4}$; $V_{Te}^2 = 2$; $\epsilon = 0.1$ and $S = 0$.

nearby modes whose frequencies drift closer together due to shear flow effects, making the modes *resonant* [48] [42] [49]. The second channel is energy exchange between *nonresonant* vortex and wave modes and between different nonresonant wave modes [40] [43].This mechanism is important at high shear rates such as those present in the LAPD experiment.

The coupling of the drift wave mode with the Alvenic-like modes is analyzed here. We start by numerically solving the three complex Eqs. (2.59),(2.61), and (2.62). Separating the real ϕ_k', n_k', ψ_k' and imaginary ϕ_k'', n_k'', ψ_k'' parts of the fields, gives

$$K_\perp^2(\tau)\frac{\partial \phi_{\mathbf{k}}'}{\partial \tau} - 2SK_x(\tau)K_y\phi_{\mathbf{k}}' = -K_\perp^2(\tau)\psi_{\mathbf{k}}'', \tag{2.64}$$

$$\frac{\partial n_{\mathbf{k}}{}'}{\partial \tau} - K_y V_{de}\phi_{\mathbf{k}}'' - \epsilon K_y V_{de}\phi_{\mathbf{k}}{}' = V_{Te}^2 v\hat{\delta}_e^2 K_\perp^2(\tau)\psi_{\mathbf{k}}'', \tag{2.65}$$

$$\left[1+\hat{\delta}_e^2 K_\perp^2(\tau)\right]\frac{\partial \psi_{\mathbf{k}}'}{\partial \tau} - 2S\hat{\delta}_e^2 K_x(t)K_y\psi_{\mathbf{k}}' = -\phi_{\mathbf{k}}'' + n_{\mathbf{k}}'' + K_y V_{de}\psi_{\mathbf{k}}'', \tag{2.66}$$

$$K_\perp^2(\tau)\frac{\partial \phi_{\mathbf{k}}''}{\partial \tau} - 2SK_x(\tau)K_y\phi_{\mathbf{k}}'' = K_\perp^2(\tau)\psi_{\mathbf{k}}', \tag{2.67}$$

$$\frac{\partial n_{\mathbf{k}}''}{\partial \tau} + K_y V_{de}\phi_{\mathbf{k}}' - \epsilon K_y V_{de}\phi_{\mathbf{k}}{}'' = -V_{Te}^2\hat{\delta}_e^2 K_\perp^2(\tau)\psi_{\mathbf{k}}', \tag{2.68}$$

$$\left[1+\hat{\delta}_e^2 K_\perp^2(\tau)\right]\frac{\partial \psi_{\mathbf{k}}''}{\partial \tau} - 2S\hat{\delta}_e^2 K_x(t)K_y\psi_{\mathbf{k}}'' = \phi_{\mathbf{k}}' - n_{\mathbf{k}}' - K_y V_{de}\psi_{\mathbf{k}}'. \tag{2.69}$$

The results from these simulations can be seen in Figs. 2.2-2.11. The parameters for each simulation, approximating the parameters of the LAPD experiments, are given in Table I. Our results reveal a novel linear effect: the

linear evolution of drift wave mode perturbations in the zonal flow excites Alfvénic-like fluctuations.

In the present case, both channels of linear coupling are at work. The fluctuations gain energy from the shear flow and experience transient growth. As the structures are stretched by the shear flow, the drift wave frequencies become comparable to the kinetic Alfvén modes and the modes couple resonantly.

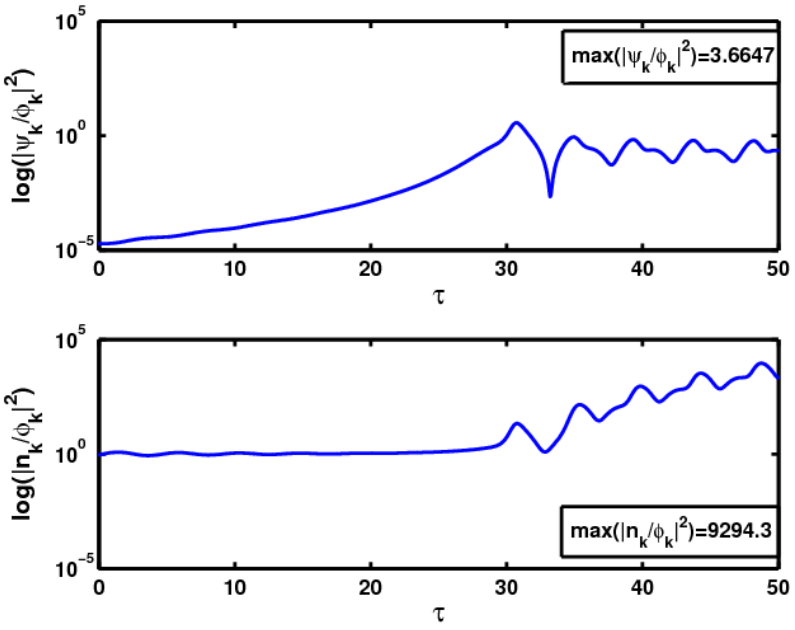

Figure 2.3: The dynamics of relations $|n_{\mathbf{k}}/\phi_{\mathbf{k}}|$ and $|\psi_{\mathbf{k}}/\phi_{\mathbf{k}}|$ for initial conditions that correspond to the pure drift wave with $K_y \ll K_x(0)$. Here $K_x(0) = 3 \times 10^4$; $K_y = 10^3$; $V_{de} = 2 \times 10^{-3}$; $\hat{\delta}_e = 5 \times 10^{-4}$; $V_{Te}^2 = 2$; $\epsilon = 0.1$ and $S = 1$ (Table I, Simulation 1). Initial conditions are defined by Eqs. (2.53)-(2.55)

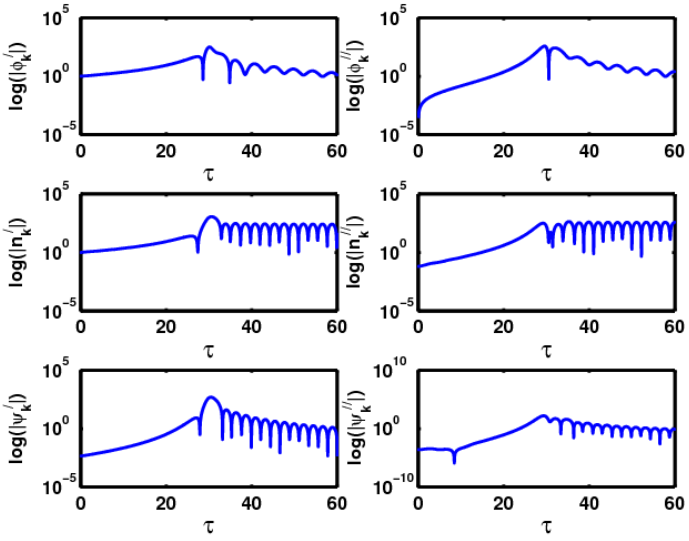

Figure 2.4: A) The evolution of a single SFH (logarithms of real and imaginary parts of normalized fields (Ψ_1, Ψ_2, Ψ_3) are shown for the same case as in Fig. 2.2.

The parallel and perpendicular kinetic, electron thermal and magnetic energies associated with the perturbations are

$$E_{kin}^{\perp}(\tau) = \hat{\rho}_s^2 K_{\perp}^2(\tau)|\phi_{\mathbf{k}}|^2, \tag{2.70}$$

$$E_{kin}^{||}(\tau) = \hat{\rho}_s^2 \hat{\delta}_e^2 K_{\perp}^4(\tau)|\psi_{\mathbf{k}}|^2, \tag{2.71}$$

$$E_n(\tau) = |n_{\mathbf{k}}|^2, \tag{2.72}$$

$$E_m(\tau) = \hat{\rho}_s^2 K_{\perp}^2(\tau)|\psi_{\mathbf{k}}|^2, \tag{2.73}$$

and the sum of all the energies, $E(\tau)$ is used as a measure of the intensity of a given spectral fourier harmonic.

It is clear from Fig. 2.6 that the initially mostly electrostatic drift wave fluctuations acquire a significant electromagnetic character around time $\tau = 30$, in units of Alfvén times.

Because of the flow shear-induced time dependence, $K_x(\tau)/K_y$ starts from small positive value to low values and on to large negative values. It can be seen in Fig. 2.6 that while $K_x(\tau)/K_y > 1$, the drift wave SFH grows substantially monotonically for a finite time period, while the magnetic fluctuations stay small ($\psi_k/\phi_k << 1$). In contrast, when $K_x(\tau)/K_y \approx 1$, significant magnetic fluctuations appear ($\psi_k/\phi_k \simeq 1$). The drift wave SFH generates the Alfvénic-like SFHs via nonresonant coupling when $K_x(\tau)/K_y \approx 1$. However, as time advances and $K_x/K_y << 0$, the drift waves again become mostly electrostatic.

It can also be seen in Fig. newenergies that during that most of the evolution, the parallel kinetic energy $E_{\rm kin}^{\parallel}(\tau)$ exceeds the magnetic energy. Both types

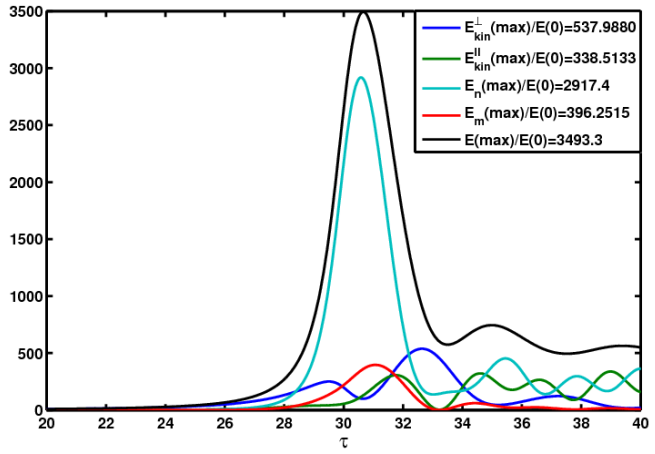

Figure 2.5: The evolution of different kinds of energies of perturbation SFH ($E_k(\tau)/E(0)$, $E_n(\tau)/E(0)$, $E_m(\tau)/E(0)$, $E(\tau)/E(0)$) for the Simulation 1 with initial conditions that correspond to a pure drift wave with $K_y \ll K_x(0)$. Here, as in Fig. 2.2, $K_x(0) = 3 \times 10^4$; $K_y = 10^3$; $V_{de} = 2 \times 10^{-3}$; $\hat{\delta}_e = 5 \times 10^{-4}$; $V_{Te}^2 = 2$; $\epsilon = 0.1$ and $S = 1$ (Simulation 1). To enlarge "the dynamically active region", the evolution is presented for times $\tau > 20$, as, initially, the growth of different energies are quite trivial: small and monotonic.

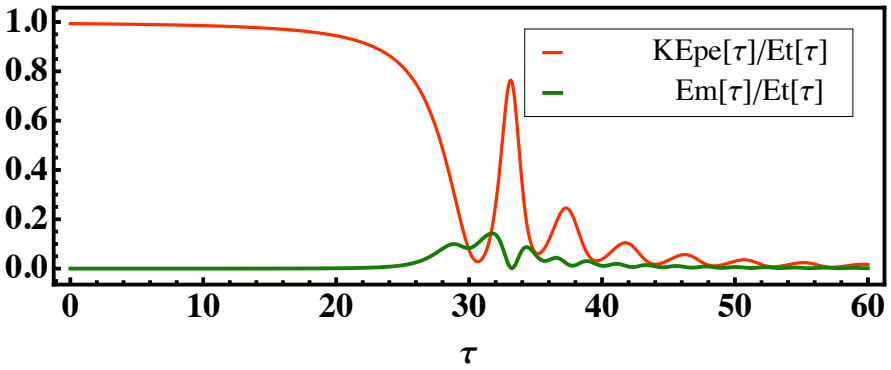

Figure 2.6: The red curve shows the energy associated with the plasma potential, $E^{\perp}_{\rm kin}(\tau)$, as a fraction of the instantaneous total energy. At $\tau = 0$, the fluctuations are drift waves with plasma potential and density fluctuations of comparable magnitude. It can be seen that for a short time around $\tau \approx 30$, the magnetic energy $E_m(\tau)$ (green curve) surpasses the $E^{\perp}_{\rm kin}(\tau)$ and the dynamics become electromagnetic.

of energies are due to the magnetic fluctuations, but $E^{\parallel}_{\rm kin}(\tau)$ is proportional $\delta_e^2 K_\perp^2$, where δ_e is the electron skin depth, which is a measure of the effect of electron inertia. Around $\tau = 30$, $E_m(\tau)$ roughly matches $E^{\parallel}_{\rm kin}(\tau)$ due to $\delta_e^2 K_\perp^2 \approx 1$, indicating that the fluctuation scale length becomes of the order of the electron inertial length.

Comparing Figs. 2.4B and 2.8C, we see that increasing V_{Te}^2 causes transient electron thermal energy and total energy growth. The magnetic energy decreases but only slightly. Looking at the differences between Fig. 2.4c-e and 2.8d, it becomes clear that the phenomenon of transient growth strongly depends on the value of flow shear, as quantified by the normalized shear parameter S. The generation of Alfvénic-like fluctuations becomes appreciable

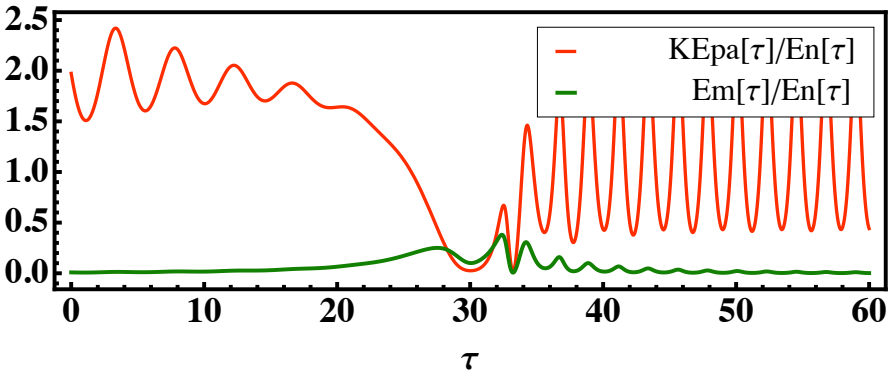

Figure 2.7: The red curve shows the energy associated with the diamagnetic drift $E^{\parallel}_{\rm kin}(\tau)$, as a fraction of the instantaneous elastic energy. When $\tau \approx 30$, the magnetic energy $E_m(\tau)$ (green curve) becomes comparable to $E^{\parallel}_{\rm kin}(\tau)$, showing that the scales become of the order of the electron skin depth .

at $S = 0.3$, pronounced at $S > 0.5$, and at the values $S = 1$ of the LAPD experiment, the generation is dominant.

2.7 Broadband spectrum and abrupt transitions

The bursts in the energies in the shear region in Figs. 2.4B - 2.8D show that fluctuations in strongly sheared flows are highly non-normal. As the evolution of poloidal flux and electron density in Fig. 2.3 shows, there is a critical moment when the evolution of the fluctuations changes abruptly. Before $\tau = 30$, the fluctuations experience nearly monotonic growth, while for$\tau > 30$, the fluctuations show a repeating bursty pattern.

The flat parts of the spectrum for frequencies beyond the $m = 17$ mode reflect a broad band of high frequency fluctuations.

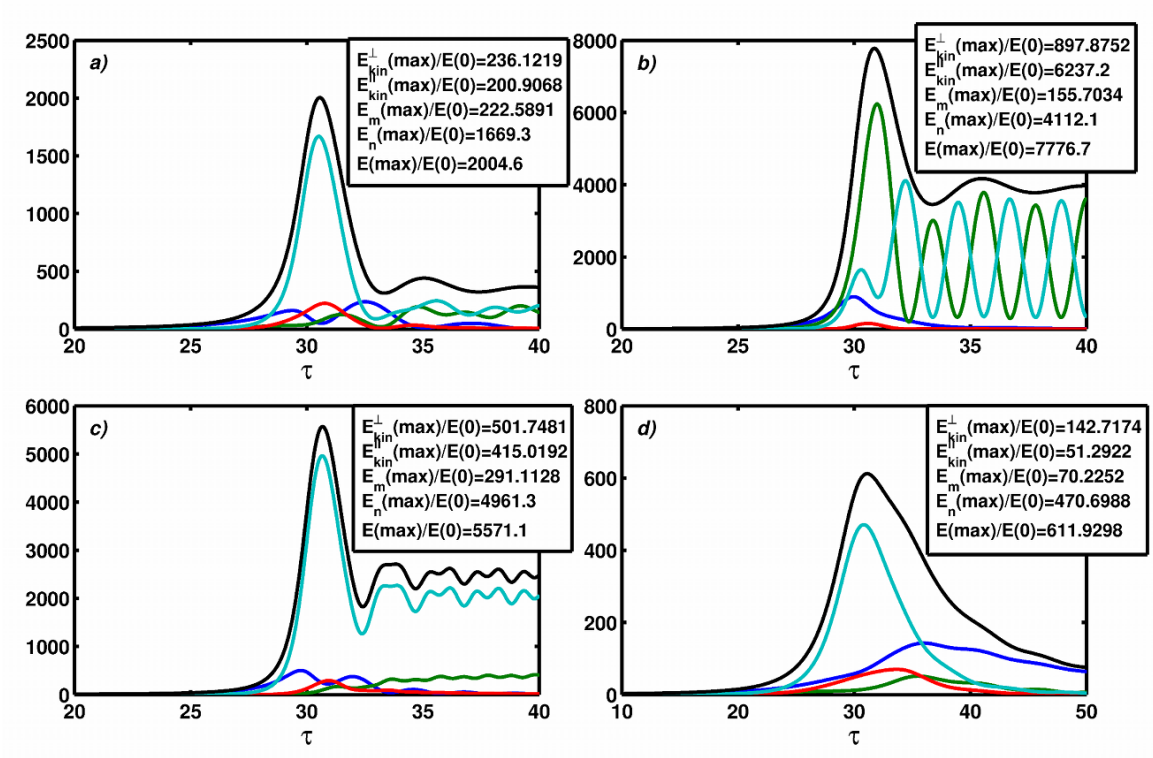

Figure 2.8: Same as previous figure, but at a) $\epsilon = 0$ (Simulation 2); b) $K_x(0) = 3 \times 10^5$ and $K_y = 10^4$ (Simulation 3); c) $V_{Te}^2 = 10$ (Simulation 4); d) $S = 0.3$ and $K_x(0) = 0.9 \times 10^4$ (Simulation 5). The evolution is presented for times $\tau > 10$.

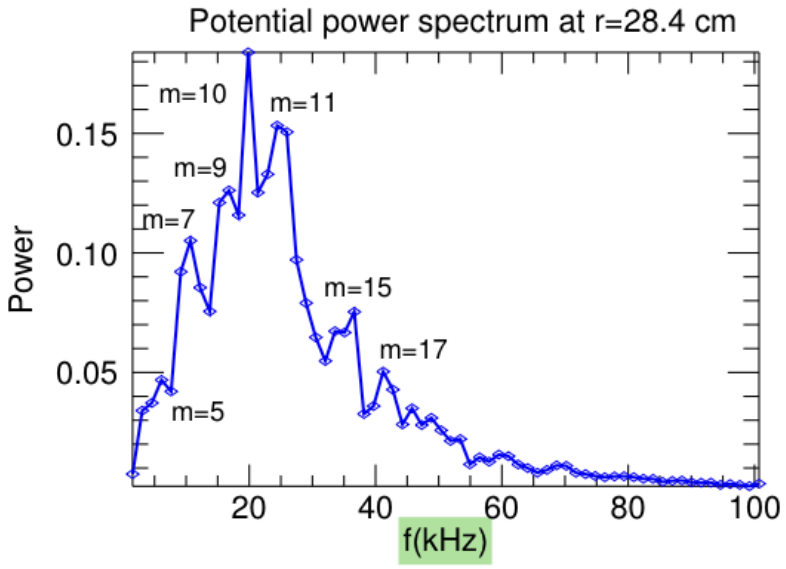

Figure 2.9: The auto power spectrum for the plasma potential at the center of the shear region. Although turbulence is dominated by the low azimuthal modes, the frequencies extend from 5 to approximately 80 kHz.

Shear non-normality coupling may have also been at work in recent JET experiments, where the magnetic turbulence changed abruptly during L-H transitions.[13]. A phase spectrograph from the JET experiment (Fig. 2.10) shows these abrupt transitions.

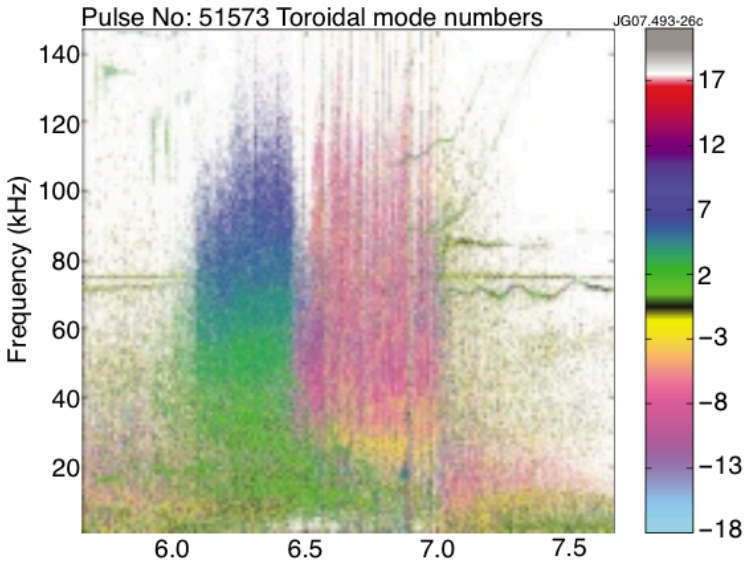

Figure 2.10: Phase spectrograph for toroidal mode numbers for JET turbulence. An internal transport barrier is triggered at 6s. There is an abrupt transition from $n \approx 1$ modes to $n \approx -5$ modes. Positive n's correspond to waves with phase velocity along the current [Sharapov, 2008].

In addtion, broad band electromagnetic waves appeared during the formation of internal and external transport barriers. The zonal flow in JET and tokamak plasmas is bipolar self-induced flow and generally weaker than the externally imposed shear flow of the LAPD experiment. Determining conclusively that these two effects in JET are due to shear-induced non-normality requires more

investigation. The evolution consisting of abrupt spectrum changes seen so clearly in JET are not expected to be observed in the LAPD experiment because the LAPD shear flow is externally imposed rather than part of self-consistently induced zonal flow.

2.7.1 Bypass transition and nonlinear interactions

Several works demonstrate the occurrence of "bypass" transition, which is the onset of turbulence in spectrally stable shear flow [50] [35] [38] [51] [52] [53] [54] [55] [56] [57] [58] [59] [60]. In the bypass transition, vortical perturbations grow transiently as energy is extracted from the basic flow through the linear non-normal mechanism, and the nonlinear terms redistribute the energy in the wavenumber space. Transiently growing perturbations can be repopulated as the energy cycles back between different modes.

The evolution of the different energies is shown in Fig. 2.4 c-e. They reveal a substantial transient burst of electron thermal energy (determined by the electron density) and the appearance of Alfvénic-like fluctuations.

2.7.2 Comparison to pure vortex mode growth

Taking the RHS of Eq. (2.59) to be zero, we can obtain the perpendicular kinetic energy evolution due to a pure vortex mode. Fig. 8 compares this (black curve) to the perpendicular kinetic energy evolution due to the full Eq. 2.59 (blue curve). The pure vortex undergoes transient growth while our present case, the perpendicular kinetic energy evolution is complicated and it

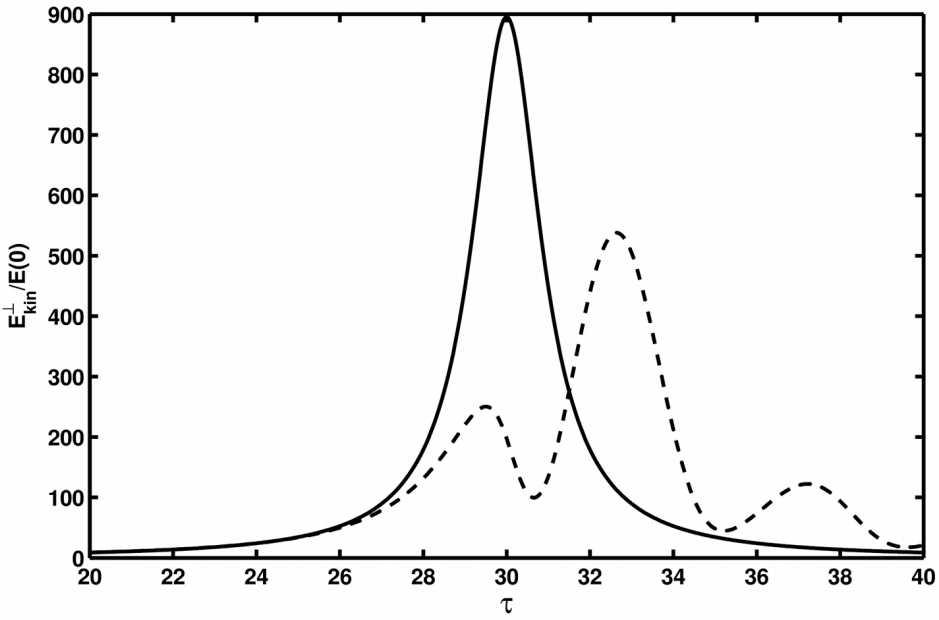

Figure 2.11: The evolution of perpendicular kinetic energy of perturbation SFH ($E_k(\tau)/E(0)$) in two different cases. The dashed line relates to the considered system for the parameters presented on Fig. 2.4 c-e. The solid line relates to the pure vortex mode case (i.e., when RHS of Eq. (2.59) equal zero). The evolution is presented for times $\tau > 20$, as, initially, the growth of energies in both cases are quite identical.

actually decreases due to the dynamics of the other fields.

2.7.3 Effect of trapped electron instability

Figure 2.2 shows that for all values of K_x, the drift wave growth rates $\omega_{Im} << 1$. For the least stable drift wave mode, the maximum frequency and growth rates are 0.9 and 0.09. The maximum frequencies occur when $\|K_x/K_y\| \leq 1$ and the drift waves are electromagnetic.

Magnetically trapped particles lead to drift wave instabilities as given by Eq. (2.62), discovered by Kadomtsev and Pogutse, 1970 and described in detail in Horton, *Turbulent Transport in Magnetized Plasmas*, 2012 [46][61]. Although no concrete value was specified for ϵ beyond the fact that $\epsilon << 1$, it can be safely concluded that the trapped particle instability has no significant influence on the linear transient dynamical phenomena. This is also evident from the evolution of different energies shown in Figs. 2.4 c-e and 2.8 a. The transient growth is only twice as strong at $\epsilon = 0.1$ than at $\epsilon = 0$. Other related works dealing with the classical dissipative regime have similarly found that the growth due to the trapped particle instability is negligible compared to the transient burst [46].

2.8 Comparison of nonmodal results to experimental data

Many works have demonstrated the importance of nonnormal effects in laboratory plasmas [62] [63] [64] [65]. In fact, in some configurations of the LAPD device, the non-normal effects are believed to dominate the turbulence [19]. This is despite the fact that it is not yet possible to directly observe isolated transient growth in LAPD experiments. One reason is that until now, LAPD has always been found in a saturated turbulent state where spectrally unstable linear modes start the turbulence before non-normal behaviors become significant. Another complication is that non-normal structures and fluctuations have time evolutions that are highly sensitive to specific condi-

tions and are difficult to predict. This is a significant source of difficulty that even the most targeted experiments cannot avoid.

2.8.1 Recent Kevin-Helmholtz Drift-wave LAPD experiment

The published version of this work uses results from a 2006 LAPD experiment whose main focus was providing the first vorticity measurements with a newly added vorticity probe. The important features of the 2006 experiment for the present work were poloidal flow with a strong piece-wise linear radial shear rate and radial density gradient with scale length comparable to the shear scale length. The initial conditions corresponded to a regime where the Kevin-Helmhotz and drift-wave instabilities can drive the turbulence.

These features are shared by an LAPD experiment done in 2012 whose results were presented by Zhou *et al.* [18]. We discuss the possible experimental signatures of shear-induced non-normal effects.

The 2012 experiment is performed for four different bias voltages; we will focus on the case with 75V bias voltage which experiences enhanced plasma confinement due to the formation of an internal transport barrier. Figure 2.12 shows that large magnetic fluctuations are generated in the shear region, like in the 2006 experiment.

In Fig. 2.13, the effect of wavenumber drift given by Eq. (2.40) may be solely responsible for the appearance of frequencies that do not corresponding to any single linear spectral mode. For wavenumbers $K_x(\tau)/K_y > 1$, the fluctuation gains energy from the shear flow. As the frequencies and wavenum-

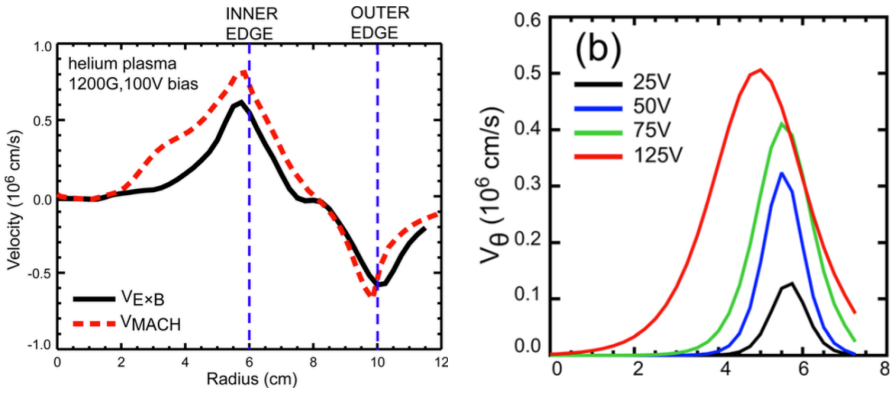

Figure 2.12: A. The poloidal velocity profile for the 2012 LAPD experiment [Zhou, 2012]. B. The large vorticity fluctuations that are generated in the shear region versus radial location.

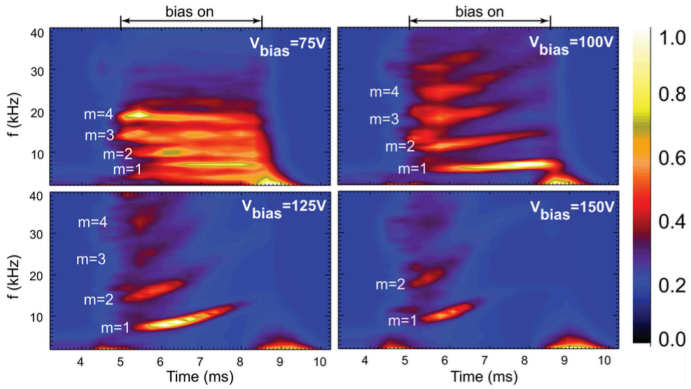

Figure 2.13: Time evolution for the power spectrum of ion saturation current fluctuations. In the 75V case (A), the spectrum begins with discrete modes. The bias has the effect of generating fluctuations of intermediate frequencies.

bers drift, modes that are linearly independent in uniform flow can become resonant. Interestingly, the spectrum of the 100V case that had bad plasma confinement shows the opposite trend. The case where a broad spectrum becomes more discrete corresponds to linear transient decay.

2.8.2 Comparison to validated nonlinear simulation

Because it is still impossible to directly prove the existence of transient growth in LAPD at this point, assertions of its existence rely on theoretical proofs of the universal features of non-normal phenomena, as well as on extrapolation from highly-controlled hydrodynamic experiments.

In an effort to make comparisons more concrete, since 2009, several groups have resorted to using nonlinear simulations as intermediaries between nonmodal calculations and the complex dynamics that take place in LAPD. Even with sophisticated simulations, the comparisons are largely of a qualitative nature because spectral simulations cannot calculate non-normal results directly. Instead, the specifics of the non-normal calculations effects are extrapolated by means of critical balance arguments.

We review one such work by Friedman *et al.* , 2014 [66]. Their work is highly relevant to our work because it focuses on induced transient growth for an almost identical set of LAPD parameters. One difference is that their initial conditions correspond to the regime where the turbulence is dominated by drift wave instability instead of the Kevin-Helmholtz drift-wave instability regime of our simulations. The effect of this difference is undermined by the fact

that, in both cases, the turbulence is found to be dominated by non-normality effects rather than by the initial spectral instability. A bigger difference is that the non-normality is taken to come from a pressure gradient rather than from shear flow.

Friedman *et al.* use a nonmodal approach to calculate an effective average growth rate spectrum due to non-normality induced transient growth of turbulent fluctuations. The direction parallel to the pressure gradient is discretized and derivatives are evaluated using finite differences. The cyclic interplay between the fluctuations and the pressure gradient that happens self-consistently in the laboratory is simulated as a series of phases. Specifically, spatially random fluctuations are allowed to gain or lose energy from the pressure gradient by means of non-normal transient growth/decay. Whether fluctuations grow or decay depends on how their wavenumber compares to the pressure gradient scale length. After some time, the transient growth/decay phase is stopped. Then, nonlinear interactions are allowed to re-randomize the fluctuations, after which the cycle is repeated. This is the Bypass transition described in subsection 2.7.1. Because there is no obvious choice for the duration of the linear growth and nonlinear energy transfer phases, several time scales are tested.

Even though spectral codes cannot deterministically include non-normality effects, codes generally contain phenomenological and numerical parameters that can be tuned to correctly reproduce experimental observations. In the work of Friedman *et al.* , a nonlinear BOUT++ code with artificial diffusion

and viscosity terms that predicts well the growth rates observed in LAPD is used to provide an expected LAPD growth rate spectrum for the conditions simulated in the nonmodal simulation. Recall that the nonmodal simulations are repeated for several time scales. The time scale that best matches the expected LAPD growth rate is taken to be the most realistic. Note that, in order to isolate the character of nonmodal behaviors, both the nonmodal simulation and the spectral simulation treat only a subset of the complex dynamics that occur in LAPD.

2.9 Conclusions and discussion

LAPD basic physics experiments report Alfvéntic-like fluctuations generated in the region with strong flow shear. A dynamical system for the evolution of the plasma density, electrostatic potential and magnetic fields in the LAPD device are analyzed using the Kelvin Nonmodal approach. In the framework of the Kelvin nonmodal appraoch, the wavenumber of the drift wave spatial Fourier harmonics $K_x(\tau)$ acquires a time-dependence due to the flow shear: beginning with low values, through zero and then to large values.The drift wave SFH grows transiently. When $K_x(\tau)/K_y < 0$, the drift waves generate Alfvénic-like wave modes, as illustrated in Figs. 2.2 and 2.4.

We show that drift waves are qualitatively affected by normalized flow shear of order unity. The combined drift wave- shear flow system experiences induced transient growth. The flow shear also leads to complex temporal wave forms and Alfvénic-like fluctuations. We consider the effect of the trapped

particle instability on the shear-induced transient growth but show that this and other classical drift wave instabilities have no significant influence on the system dynamics on the Alfvénic time scales for the parameters of the LAPD experiments. The energy exchange between different modes at high shear rates is shown to include both resonant and nonresonant linear mode coupling. The agreement of the presented simulations with the LAPD experiment measurements suggests that this mechanism may account entirely for the previously unexplained magnetic fluctuations that were observed in LAPD.

Zonal flow plays important roles in magnetically confined plasmas in the laboratory and in space and thoroughly understanding shear-flow phenomena is essential to achieving record confinement times and power output in fusion experiments. In the laboratory, zonal flow is widely used to produce local transport barriers and to dampen turbulence. The shear-induced nonmodal behavior presented here is universal at high zonal flow shear rates and it should also occur around rational surfaces in Tokamaks, where the shear parameter peaks. Future work will account for the subtler features of Tokamak zonal flow configurations.

Chapter 3

Evolution of Bounded Plasma Jet

3.1 Introduction

Magnetized plasma jets have emerged as one of the two canonical systems used to study magnetofluids [4]. Generally, magnetofluids are plasmas with a sheared flow field and a sheared magnetic field in close proximity [10]. There are many interesting laboratory plasmas experiments with combined flows and magnetic shear, including the Helimak [67] and the LAPD [17] experiments.

In a magnetized plasma jet, a localized flow perpendicular to the ambient magnetic field is superimposed on the sheared magnetic field. Such systems have been used to model solar surges [5] [6] and the fast flows in Earth's magnetotail [7]. In addition, magnetized jets are closely related to magnetized plasma wakes, which, in turn, have been used to model the heliospheric current sheet [8], slow solar wind [68], and nonthermal galactic jets [69].

Magnetized jets have been studied widely because they occur in many systems of physical interest. Many occurrences of magnetized jets are in systems of large spatial extent, such as astrophysical plasmas. Because boundary effects can usually be ignored in these systems, these jets are treated as un-

bounded, and the effects of the boundaries remain largely unstudied. Magnetized jets occur in smaller systems such as in laboratory plasmas, and there, the magnetic and flow fields can significantly interact with boundaries. We carry out calculations of a bounded mangetized jet to explore the effect of boundaries on different modes, on stability, and on turbulence production. The results will be related to an earlier study of unbounded magneitzed jets [4]. The findings also inform how other magnetofluids are affected by boundaries, especially laboratory plasmas. This work is published in Dahlburg *et al.* [11].

Features included in our model are three spatial dimensions, resistivity, viscosity, and two boundaries consisting of no-slip walls. We compare the results to measurements from the Helimak device, which, in addition to the features included in the calculations, has a toroidal magnetic field and a controlled poloidal velocity flow that resembles a bounded jet [4]. The ideal sinuous mode that occurs in unbounded magnetized jets persists in the bounded jet. In contrast, the bounding walls are found to stabilize the ideal varicose modes. Reynolds and Maxwell stresses, and sheared magnetic fields near walls have all been shown to influence the stability of some magnetized flows [70]. We perform an energy-stress analysis that reveals that the Maxwell stress is crucial for the growth of the instability.

3.2 Review of unbounded magnetized jets

The unstable modes that have been found to appear in unbounded jets are ideal, dissipationless instabilities of large cross-stream spatial extent, that could, therefore, be affected by walls. For instance, walls can disrupt the structure of modes. Walls can produce large stresses that will affect the fluid velocity and magnetic field structures.

3.2.1 Relation to magnetized wake field

A magnetized jet can be transformed into a magnetized wake field by a Galilean transformation with respect to the maximum jet speed. Therefore the literature on magnetized wakes can be applied to magnetized jets. These systems have been studied in two limits: the flow-dominated limit (Alfvén number $|A| \leq 1$, where $A \equiv V_A/V_0 = 1/M_A$, V_A is the characteristic Alfvén speed, V_0 is the characteristic flow speed and M_A is the Mach number.) and the magnetic field-dominated limit $A > 1$. In unbounded flow dominated systems, two unstable modes have been found that are an ideal varicose mode and a sinuous mode. In varicose modes, the cross-stream flow is antisymmetric about the point of maximum or minimum flow and in sinuous modes, the cross-stream flow is symmetric. In magnetic-field dominated jets, the ideal modes are stabilized and a resistive varicose mode appears.

For magnetized jets and wakes, the Reynolds stress, Maxwell stress and cross-field stress all influence the energetics. The value of the stress components and the direction of energy flow also vary with the Alfvén number.

Within the nonlinear incompressible limit, three unstable modes occur, but only at large Alfvén numbers.

3.3 Helimak configuration and parameters

This study focuses on the linear stability of a bounded jet for the configuration of the Helimak device and three different flow profiles produced by it. The Helimak is a toroidal magnetic confinement device at The University of Texas at Ausin that produces sheared magnetic field slab geometry. This configuration is widely used by theorists to study localized modes in Tokamaks [67]. Two schematics of the experiment geometry and the coordinate system adopted in this study are shown in Fig. 3.1. Plasma flows through two concentric cylinders with conducting walls located at $r = a = 0.6$m and $r = b = 1.6$ m. A set of 16 toroidal field coils around the vacuum chamber produce a dominant toroidal field B_ϕ of order 0.1 T. A weaker vertical field B_z of order 0.01 T is produced by three poloidal field coils. The ratio of toroidal to poloidal field can be changed by changing the current flowing through the coils. The resulting helical field spirals from bottom to top, with a pitch varying with radius because the toroidal field decreases as $1/r$, and the field has a continuum of field line axial lengths $L_{||}$. Varying the value of the vertical field B_z can move that range of lengths from 20 m to 1 km.

The plasma is singly ionized Argon with electron peak temperature $T_e = 10$eV and the ratio of thermal to magnetic energy densities is $\beta = m_i\beta_e/m_e \approx 1 - 2$, where β_e is the corresponding ratio for the electrons. The

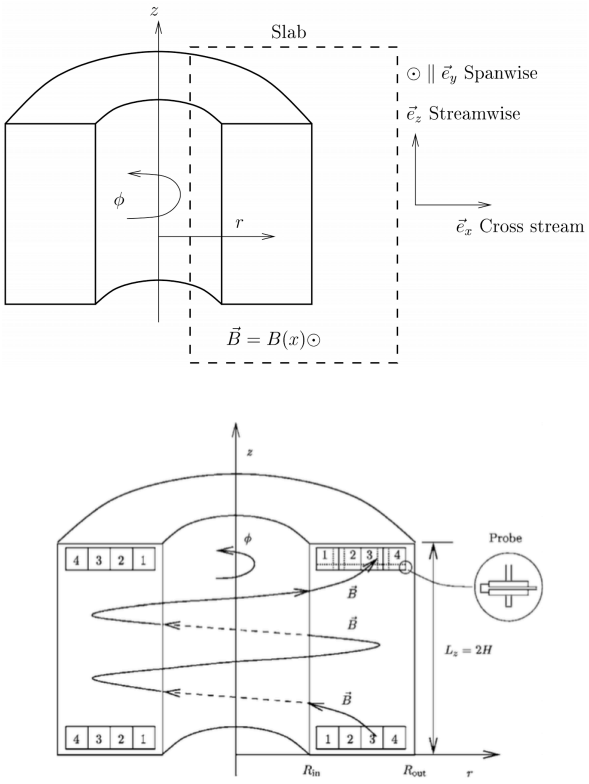

Figure 3.1: Schematic drawings of the Helimak illustrating the coordinate system used in this paper and a magnetic field line.

plasma density ranges from 2×10^{16} to 2×10^{17} cm^{-3}. The Alfvén velocity is $V_A = 1-3\times10^8$ cm/s, the resistivity is $\eta = 10^{-5}$ Ωm and the kinetic viscosity is $\nu = 10^4$ cm^2/s. For a magnetic Reynolds number defined as $S = V_A a/(\eta/mu_0)$ and a viscous Reynolds number $S_\nu = V_A a/\nu$, their values are both taken to be 5000 for the baseline case. The plasma column has a height $H = 2$m and magnetic field lines of length $L = B_\phi H/B_z > 50$m, giving Alfvén frequency $k_{||}v_A/(2\pi) \approx 10$ kHz. For this study, the toroidal and vertical magnetic fields have a ratio of $B_\phi/B_z \approx 0.1$ T/0.01 T ≈ 10 at midradius $r \approx 1.1$m from the vertical symmetry axis.

The Helimak configuration can be classified as a bounded magnetized plasma jet. Because the Helimak can have long helical magnetic field structures with wavelengths as long as 100m, Alfvén wave modes and magnetic field fluctuations play an important role in the dynamics.

A bias voltage on segmented end plates produces a localized cross-field electric field E_r, modifying the flow profile. We will analyze three different vertical flow configurations that are produced in the Helimak plasma. The localized E_r leads to $\mathbf{E} \times \mathbf{B}$ drift, resulting in a localized high speed plasma stream along the axial direction. The values of the bias voltage V_{bias} are given in Fig. 3.2, and the resulting velocity $v_z = w(x)$ profiles are shown. Velocity measurements are made via spectroscopic Doppler shift of singly ionized Argon lines. The associated normalized vorticity dV_z/dr is of order 5×10^3. The parameters of the Helimak experiment are summarized in Table I.

The electric potential and electron density fluctuation amplitudes are

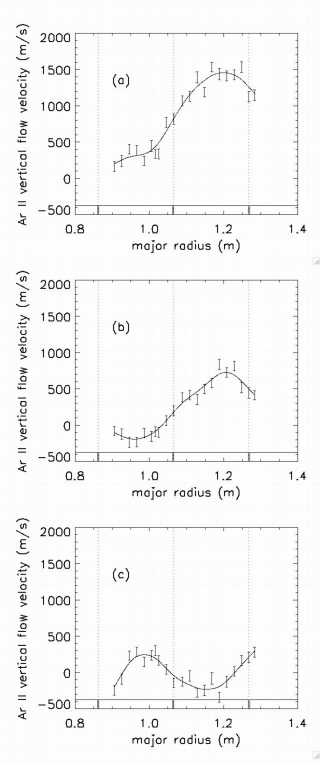

Figure 3.2: Profiles of vertical flow velocity $v_z = w(x)$ produced in the Helimak device using bias voltages A.) $V_{\text{bias}} = 0$, B.) $V_{\text{bias}} = -10$ V, and C.) $V_{\text{bias}} = -15$ V. Values are measured using Doppler shift spectroscopy of spectral atomic emission lines of singly ionized argon.

measured with Langmuir probes and shown in Fig. 3.3.

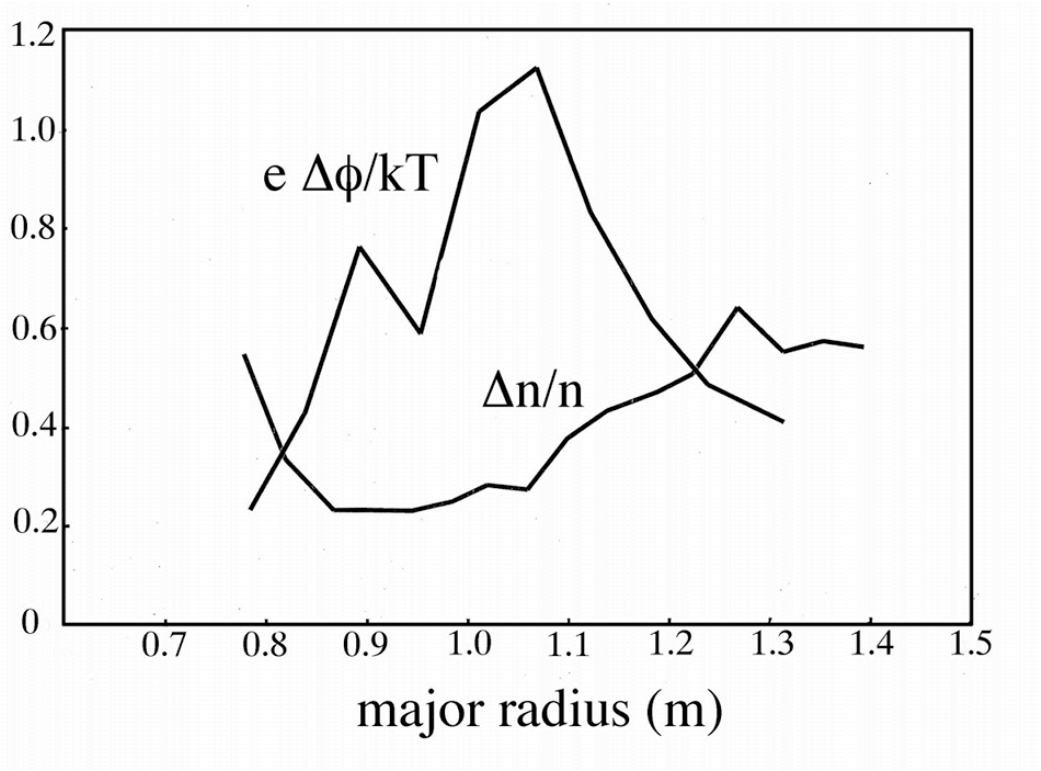

Figure 3.3: Langmuir probe measurements of the electric potential and the electron density in a 10eV argon plasma [Gentle, 2008].

3.4 Model equations

The equations include terms for resistivity and viscosity. The density fluctuaions are small compared to the dimensionless potential fluctuations, therefore the plasma behaves approximately as an incompressible resistive-visous MHD fluid. The drift wave terms are dropped because the electron flow

velocity is large compared to the drift velocity. In this weakly compressible regime, Ohm's law simplifies to $E_{||} = \eta j_{||}$.

We adopt the the Helimak configuration to determine its principal modes of evolution. The plasma is contained in a channel that can be modeled as a slab inside the Helimak. The slab geometry used for this model can be seen in Fig. 3.1. The origin of the slab coordinate system is at the center of the channel. The x-axis lies along the radial direction, and x is allowed to vary from -1 to 1. The toroidal direction is represented by the y' axis and the axial direction is represented by the z' axis. The equations are written in a frame of reference rotated to align with the helical field. The streamwise direction is denoted by the unprimed y and the spanwise by the unprimed z.

3.4.1 Boundary conditions

The conducting walls are modeled as no-slip in the x-direction. In the y' and z' directions, periodic boundary conditions are used. Therefore the perturbed flows u', v', w' in the x, y' and z' directions, respectively, are

$$u'(x = \pm 1) = v'(x = \pm 1) = w'(x = \pm 1) = 0, \tag{3.1}$$

The toroidal field produced by external coil currents is modeled as

$$B_\phi = \frac{B_0 R_0}{r} = \frac{2aB_0}{b + a + (b - a)x}. \tag{3.2}$$

For $B_\phi(x = -1) = B_0$, in the local coordinates

$$\mathbf{B'}_{0y'}(x) = \frac{1.2}{2.2 + x}\hat{\mathbf{e}}_{y'}, \qquad \mathbf{B'}_{0z'} = 0.1\hat{\mathbf{e}}_{z'}, \tag{3.3}$$

The localized vertical plasma stream has velocity $W' = E_r/B_\phi = W'_0(x)$ and is modeled with a hyperbolic cosine function $\mathrm{sech}(r - r_0/w) \to \mathrm{sech}(3x)$. In local coordinates, the baseline flows in the y' and z' directions are

$$\mathbf{V'}_0 = 0.0\hat{\mathbf{e}}_{y'}, \qquad \mathbf{W'}_0(x) = 0.1\frac{\mathrm{sech}(3x) - \mathrm{sech}(3)}{\mathrm{sech}(0) - \mathrm{sech}(3)}\hat{\mathbf{e}}_{z'}, \tag{3.4}$$

and they are shown in Fig. 3.4.

3.4.2 Rotation to field-aligned coordinates

The magnetic field in the Helimak is helical, with a pitch angle of $\theta \approx -10.56$. By rotating the y'-z' plane by this angle, we can isolate the sheared magnetic field in the y-direction. In the rotated system, we have the streamwise and spanwise coordinates y and z, velocity vector $\mathbf{v'} \to \mathbf{v}$, magnetic field $\mathbf{B'} \to \mathbf{B}$, and wavenumbers $\mathbf{k'} \to \mathbf{k}$ that satisfy $\mathbf{k} \cdot \mathbf{B}(x = 0) = 0$. In both systems, the x-axis points in the cross-stream direction. Because the angle of rotation is small, the y and z directions are nearly aligned with the toroidal and poloidal directions, respectively. In the field-aligned coordinates, there is a continuum of Alfvén modes with $\omega = k_{||}v_A$, of which the first to go unstable are often centered at $k_{||} = 0$.

The profiles of the rotated fields, $B_{0y}(x)$ and $B_{0z}(x)$ are plotted in Fig. 3.4, along with the velocities in the y and z directions. The form of the the flow and magnetic fields in the y direction, B_{0y} and V_0 have approximately the form of a bounded magnetized jet. Looking at B_{0y} and V_0 in Fig. 3.4, the characteristic flow speed exceeds the characteristic Alfvén speed, suggest-

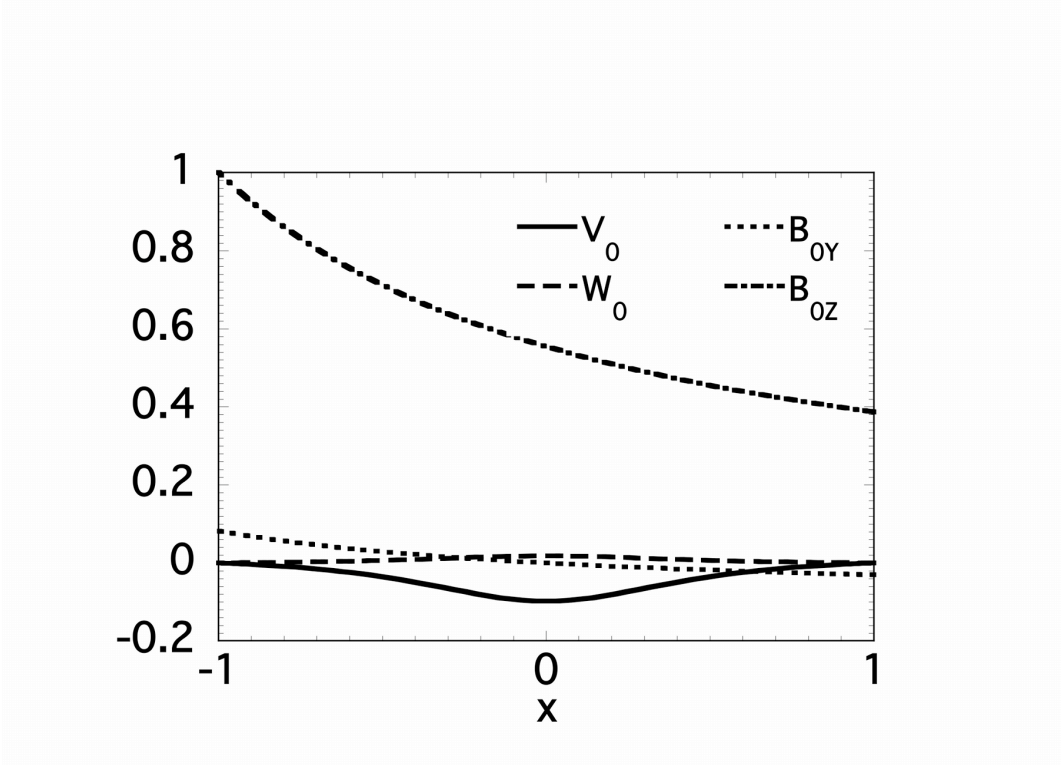

Figure 3.4: The basic flow and magnetic field profiles used in the calculations in the rotated frame of reference. In the field-aligned frame of reference, rotated by an angle $\theta \approx -10.56^\circ$, x corresponds to the radial direction; y corresponds to the the streamwise (nearly toroidal) direction; and z corresponds to the spanwise (nearly axial) direction. (Since most of our research in performed in a rotated frame of reference, we use primes to denote the laboratory frame of reference). Note that the maximum flow speed is 1/10th of the maximum Alfvén speed.

ing that the dyamics may be flow-dominated. However, the large z-direction magnetic guide field will also have a large effect.

Important differences between an unbounded magnetized jet and its bounded counterpart include the rigid boundaries and the fact that the magnetic field is not symmetric across $x = 0$.

3.5 Linear model equations

The problem of linear two-dimensional viscous parallel flow in fluid dynamics is described by the Orr-Sommerfeld equation. It is an eigenvalue equation derived from the linearized Navier-Stokes equation, and it determines the conditions for hydrodynamic stability. The channel walls are represented as two no-slip boundaries. Even in the absence of electrodynamic effects, all but the simplest velocity profiles require numerical or asymptotic methods.

The characteristic velocity is the Alfvén speed V_A; the length is normalized by the channel half-width l; and the characteristic time is taken to be l/V_A. In dimensionless form, the MHD equations are

$$\frac{\partial \mathbf{v}}{\partial t} = \mathbf{v} \times \boldsymbol{\zeta} - \nabla \Pi + \mathbf{j} \times \mathbf{B} + \frac{1}{S_\nu} \nabla^2 \mathbf{v}, \tag{3.5}$$

and,

$$\frac{\partial \mathbf{B}}{\partial t} = \nabla \times (\mathbf{v} \times \mathbf{B}) + \frac{1}{S} \nabla^2 \mathbf{B}, \tag{3.6}$$

where $\mathbf{v}(\mathbf{x}, t)$ is the flow velocity, $\boldsymbol{\zeta}(\mathbf{x}, t)$ is the vorticity, and $\mathbf{j}(\mathbf{x}, t)$ is the electric current density. We use the constraints $\boldsymbol{\nabla} \cdot \mathbf{v} = 0$ and $\boldsymbol{\nabla} \cdot \mathbf{B} = 0$,

and include both the mechanical pressure and kinetic energy density per unit mass are in $\Pi(\mathbf{x}, t)$. The resistivity and viscosity are assumed to be constant and small, with values corresponding to magnetic Reynolds number $S = 5000$ and viscous Reynolds number$S_\nu = 5000$. The plasma is highly fluid and conducting.

The Hall effect term is negligible for the low ion temperature of this experiment. Using $(\vec{v} - \vec{j}/en_e) \times \vec{B} = \vec{v} \times \vec{B} - (k_B T_e/e)\nabla \ln n_e$, Ohm's law for isothermal electrons becomes $\mathbf{E} = \eta\mathbf{j} - (k_B T_e/e)\nabla \ln n_e$ and the pressure gradient drops out of Eq. (3.6) when we take the curl.

We expand the first-order field perturbations in terms of their streamwise and spanwise wavenumbers α, β and a complex growth rate ω as

$$a_1(x, y, z, t) = a(x)\ e^{i\alpha y + i\beta z - i\omega t}. \tag{3.7}$$

Using the fact that the flow and magnetic field are divergence-free, $\boldsymbol{\nabla} \cdot \mathbf{v} = \boldsymbol{\nabla} \cdot \mathbf{B} = 0$ and linearizing Eqs. 3.5 and 3.6, give the following equations for the cross-stream perturbed velocity u and magnetic field b_x

$$\hat{\xi}^2 u - iS_\nu F\hat{\xi}u + iS_\nu(D^2 F)u = -i\omega S_\nu \hat{\xi}u + iS_\nu[(D^2 G)b_x - G\hat{\xi}b_x], \tag{3.8}$$

$$(\hat{\xi} - iSF + i\omega S)b_x = -iSGu, \tag{3.9}$$

The equations are written in terms of the operators $D \equiv d/dx$ and $\hat{\xi} = D^2 - (\alpha^2 + \beta^2)$. The boundary conditions are $u(x = \pm 1) = Du(x = \pm 1) = b_x(x = \pm 1) = 0$. The primary equilibrium velocity and magnetic fields are $F = \alpha V_0 + \beta W_0$ and $G = \alpha B_{0\mathrm{y}} + \beta B_{0\mathrm{z}}$. The solenoidality conditions can be used to determine $b_y,\ b_z,\ v$ and w.

The equations for the vorticity and electric current are

$$(\hat{\xi} - i\alpha S_\nu F)\zeta + i\alpha S_\nu G\chi = -i\omega S_\nu \zeta - \beta S_\nu[(DQ)v - (DP)b_y], \quad (3.10)$$

$$(\hat{\xi} - i\alpha SF)\chi + i\alpha SG\zeta = -i\omega S\chi - \beta S[(DQ)b_y - (DP)v]. \quad (3.11)$$

where $P = \beta B_{0y} - \alpha B_{0z}$ and $Q = \beta V_0 - \alpha W_0$ are the primary perturbed vorticity and electric current. The boundary conditions are $\zeta(x = \pm 1) = \chi(x = \pm 1) = 0$.

3.5.1 Chebyshev-τ solution of 3D eigenfunction

The eigenfunctions can be obtained by solving the perturbed vorticity and electric current Eqs. 3.10 and 3.11 for the no-slip boundaries. The linear system is solved numerically by expanding the basic and perturbed fields spectrally in three directions. Since the x-direction has no-slip boundary conditions, that direction is expanded as a truncated Chebyshev series [71] [72] [73]. The calculations are performed on the LCP&FD SGI Origin 3400 Computer. The four Chebyshev expansions are given by

$$F(x) = \sum_{n=0}^{N} \tilde{F}_n T_n(x) \quad \text{and} \quad G(x) = \sum_{n=0}^{N} \tilde{G}_n T_n(x) \quad (3.12)$$

$$u(x) = \sum_{n=0}^{N} \tilde{v}_n T_n(x) \quad \text{and} \quad b_x(x) = \sum_{n=0}^{N} \tilde{b}_n T_n(x) \quad (3.13)$$

where $T_n(x)$ represents the nth Chebyshev polynomial of the first kind, and the terms preceeding it are the expansion coefficients for each field. In the bounded jet, the magnetic field in the inner boundary is about three times larger than at the outer boundary. Accounting for this lack of symmetry

requires keeping all of the Chebyshev polynomials. Equations 3.8 and 3.9 are satisfied by exprssions 3.12 and 3.13 in the limit $N \to \infty$ but are truncated at N because they are spectrally convergent. Equation 3.8 then provides equations for $n = 0$ to $N-4$and Eq. (3.9) provides equations for $n = 0$ to $N-2$. Typically, as part of the Galerkin method, the Chebyshev polynomials are required to meet the boundary conditions. However, we use the τ-approximation method [74], wherein the boundary conditions are enforced by including the boundary condition equations themselves.

The eigenvalue problem consists of solving for the vector $\mathbf{x} = (\tilde{v}_0, \tilde{v}_1 ... \tilde{v}_N, \tilde{b}_0, \tilde{b}_1 ... \tilde{b}_N)$ and the nonsymmetric $(2N + 2)$ by $(2N + 2)$ matrices A and B that satisfies $\overleftrightarrow{\mathbf{A}}\mathbf{x} = \omega\overleftrightarrow{\mathbf{B}}\mathbf{x}$.

We use both the global and local methods to determine the eigenvalues. For the global method, the QR algorithm [75] is used to solve $\overleftrightarrow{\mathbf{C}}\mathbf{x} = \omega\mathbf{x}$. This allows us to solve for the full spectrum of eigenvalues and to identify the most unstable eigenmode. Then we use the local method to refine the eigenvalue and to compute the form of the eigenfunction. This method is also useful for parametric studies such as testing the solution's dependence on the magnetic Reynolds number.

3.6 Spectrum, eigenfunctions and dispersion relations

The parameters of the baseline Helimak case are $\alpha = 2.3$, $\beta = 0.0$, $S = 5000$, $S_\nu = 5000$. Fig. 3.5 shows the resulting eigenvalue spectrum. In this case with basic streamwise flow, there are a large number of damped, traveling

modes and one unstable traveling mode. Fig. 3.6 shows its eigenfunction. It can be seen that the streamwise components of the basic fields are those of a magnetized jet and the magnetic and flow velocity fields are of comparable amplitude.

Hence in the rotated frame of reference we have for the magnetic field:

$$B_{0\mathrm{y}}(x)\hat{\mathbf{e}}_{\mathrm{y}} = B'_{0\mathrm{y}'}\hat{\mathbf{e}}_{\mathrm{y}'}\cos\theta + B'_{0\mathrm{z}'}\hat{\mathbf{e}}_{\mathrm{z}'}\sin\theta, \tag{3.14}$$

and

$$B_{0\mathrm{z}}(x)\hat{\mathbf{e}}_{\mathrm{z}} = -B'_{0\mathrm{y}'}\hat{\mathbf{e}}_{\mathrm{y}'}\sin\theta + B'_{0\mathrm{z}'}\hat{\mathbf{e}}_{\mathrm{z}'}\cos\theta, \tag{3.15}$$

and for the flow field we have

$$V_0(x)\hat{\mathbf{e}}_{\mathrm{y}} = V'_0\hat{\mathbf{e}}_{\mathrm{y}'}\cos\theta + W'_{0\mathrm{z}'}\hat{\mathbf{e}}_{\mathrm{z}'}\sin\theta = W'_{0\mathrm{z}'}\hat{\mathbf{e}}_{\mathrm{z}'}\sin\theta, \tag{3.16}$$

and

$$W_0(x)\hat{\mathbf{e}}_{\mathrm{z}} = -V'_0\hat{\mathbf{e}}_{\mathrm{y}'}\sin\theta + W'_0\hat{\mathbf{e}}_{\mathrm{z}'}\cos\theta = W'_0\hat{\mathbf{e}}_{\mathrm{z}'}\cos\theta, \tag{3.17}$$

The unstable modes in unbounded magnetized jets are ideal sinuous, ideal varicose and resistive varicose. For the Helimak fields, that more closely resemble a bounded magnetized jet, the two varicose modes are not found. The only instability found is a sinuous mode, which is different from the sinuous mode found in the unbounded magnetized jet [4] in that it is suppressed near the inner wall, where the streamwise magnetic field is enhanced. This mode is "ideal" in the sense that neither resistivity nor viscosity are needed for it to develop.

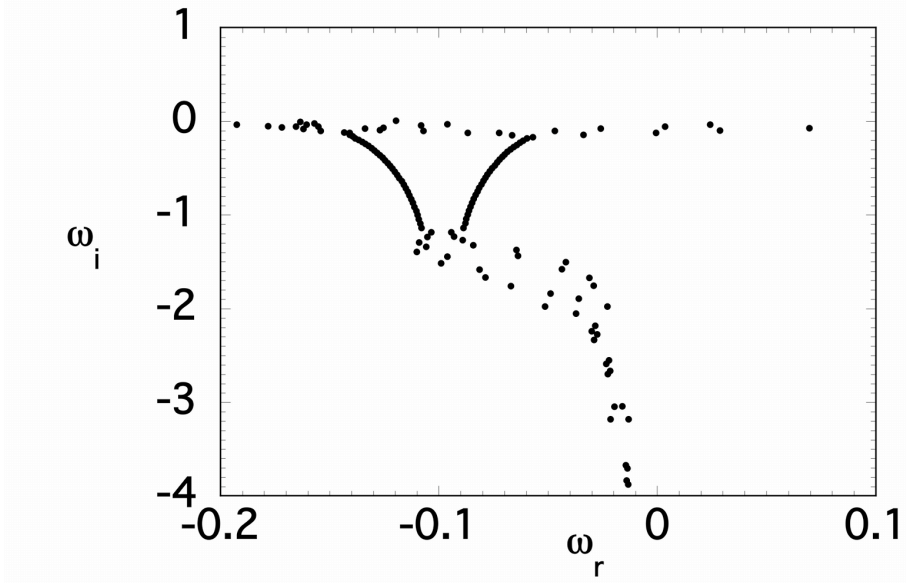

Figure 3.5: The complete eigenmode spectrum from Eqs. (3.8) and (3.9). They are solved for a typical axisymmetric vertical mode($\alpha = 2.3, \beta = 0.0, S = S_v = 5000$) for the reference flow profile given in Equations (3.14) - (3.17).

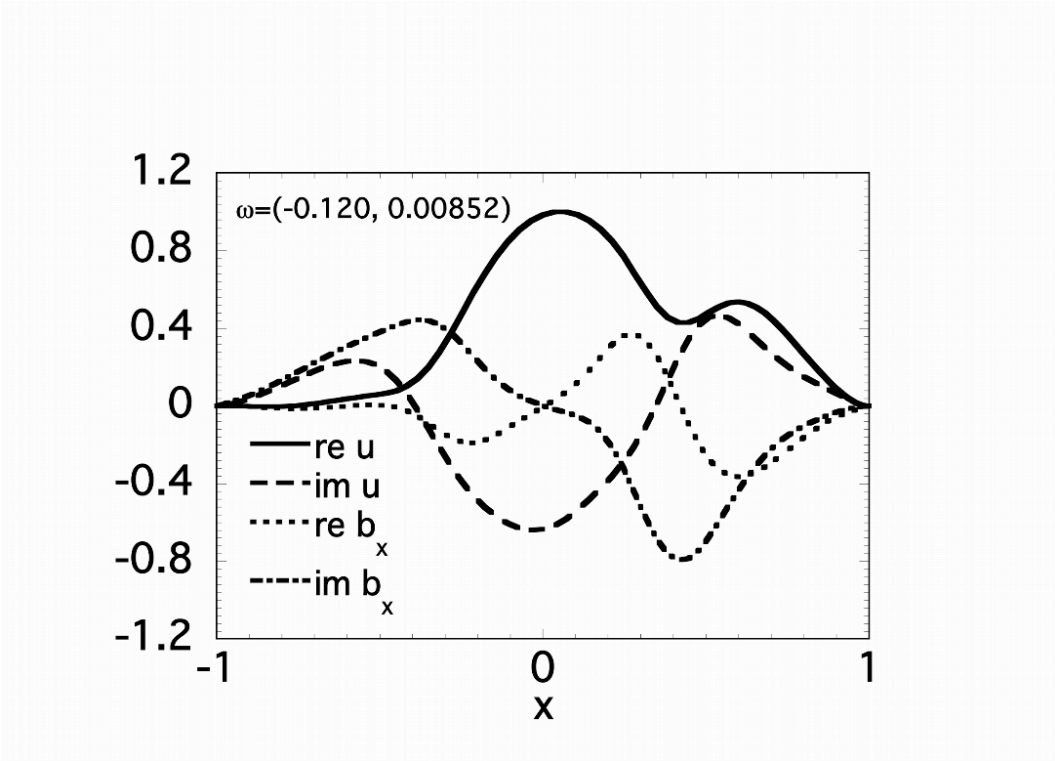

Figure 3.6: The unstable sinuous-like eigenfunction for the bounded magnetized jet ($\alpha = 2.3, \beta = 0.0, S = S_v = 5000$). For Helimak parameters, the eigenmode has an angular frequency of 2×10^5 rad/s, a growth rate of 1.4×10^4 s^{-1} and it propagates perpendicular to the helical magnetic field at $x = 0$. This eigenmode, with $k_y = \alpha/r = 4.6$ m$^-1$, is well into the resistive mhd regime, where $k_y \rho_s = 0.014$.

It is clear from the dispersion relation shown in Fig. 3.7 and 3.8 that there are cutoffs for low-α, due to the presence of channels of finite width, and for high-α, due to finite dissipation. The growth rate generally decreases with increased β. In addition, increasing β shifts the maximum growth rate value to a larger value of α. There is also a cutoff value of the spanwise wavenumber β_c above which the mode becomes stable. This suggests the possiblity of a Squires theorem for this configuration [76] [77] [78][79]. It can also be seen that the values of α and β chosen for the baseline case produce the largest growth rate for the given S and S_ν.

3.7 Effects of resistive and viscous dissipation

To understand how viscous and Ohmic dissipation affect the unstable ideal sinuous mode, we plot the variation of growth rate with the magnetic Reynolds number, parametrized by the Reynolds number in Fig. 3.9. The values accessible to the Helimak are $10^3 \leq S \leq 10^4$ and $10^3 \leq S_\nu \leq 10^4$. For the curve corresponding to $S_\nu = 2500$, the growth rate increases with S from $S = 1000$ to 1500 then decreases very gradually out to $S = 10^4$. For larger values of S_ν, the curve is similar but the growth rate is smaller. Thus, resistivityand viscosity slow the rate of growth and the effect is more significant at low values of S and S_ν. In Fig. 3.10, the strong effect of S_ν on the growth rate is shown. The mode is stabilized at $S_\nu \approx 1500$ and the growth rate increases monotonically with S_ν, flattening considerably beyond $S_\nu \approx 5000$. Viscosity has a strong damping effect over a large range of values, while resistivity only

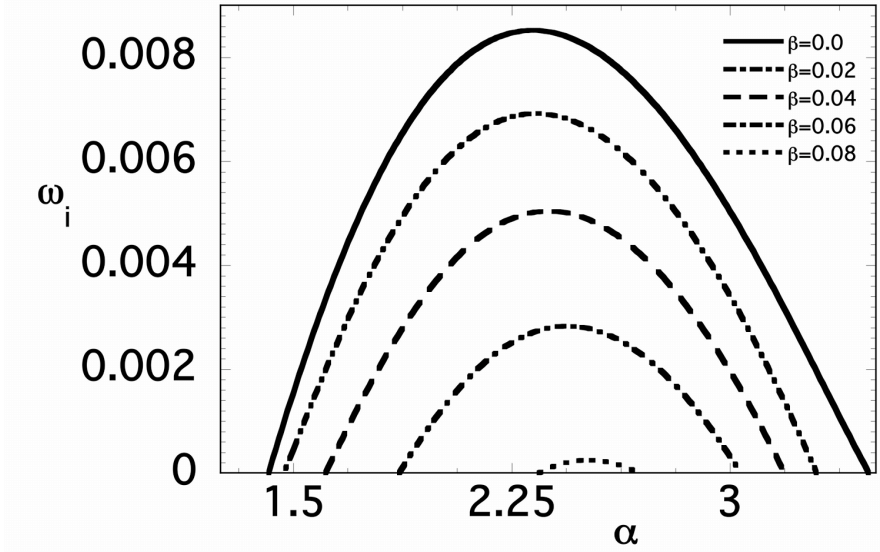

Figure 3.7: Dispersion relations for the two-dimensional case for different values of the spanwise wavenumber ($\beta = 0$). For these calculations $S_v = S = 5000$ and the wavenumber is normalized by the inverse of the channel half-width l.

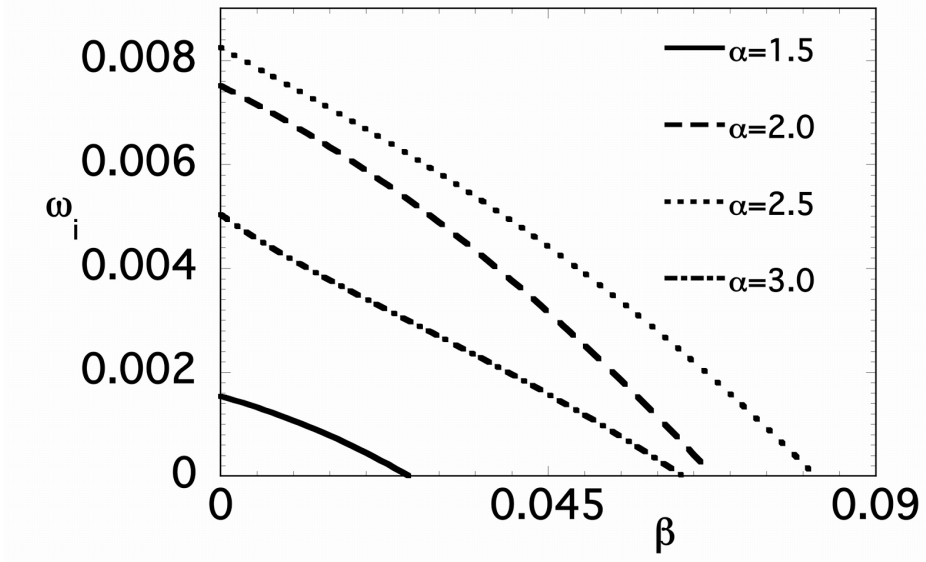

Figure 3.8: Variation of growth rate with respect to spanwise wavenumber for different values of the streamwise wavenumber (α). For these calculations$S_v = S = 5000$.

has a slight damping effect at small values of S.

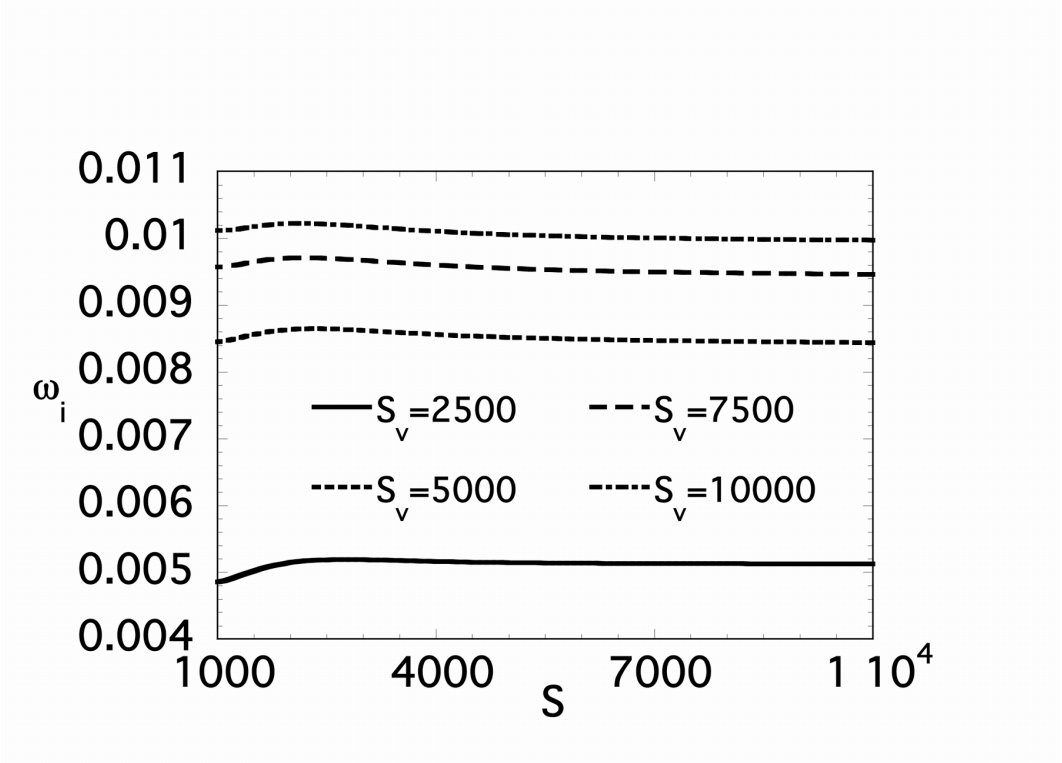

Figure 3.9: Variation of growth rate with respect to magnetic Reynolds number (S), calculated using $\alpha = 2.3$ and $\beta = 0.0$ and a set of different values of the viscous Reynolds number (S_v). The growth rate is defined as $\omega_i = Im(L\omega/v_A)$ and $\gamma \approx 10^4$/s according to the parameters in Table I.

3.8 Discussion

We examined various ways in which the presence of walls can affect the evolution of magnetized jets. Calculations are carried out for the Helimak configuration and parameters. Indeed, bounded magnetized jets evolve differ-

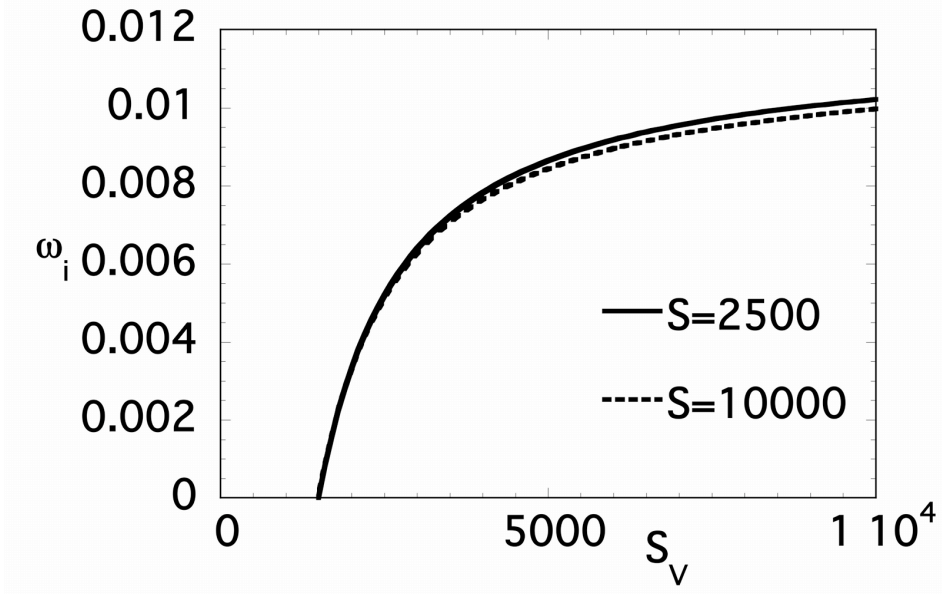

Figure 3.10: Variation of growth rate with respect to viscous Reynolds number (S_v) for different values of the magnetic Reynolds number (S). These calculations use $\alpha = 2.3$, $\beta = 0.0$, and $\omega_i = Im(L\omega/v_A)$.

ently than unbounded magnetized jets. Only one unstable mode was found, corresponding to an ideal sinuous mode that is similar but not equal to the unstable sinuous mode found for unbounded magnetized jet [80]. The laboratory signature of this sinuous mode is the presence of correlated magnetic and flow fluctuations that grow with the strength of the flow shear and its curvature. This mode has upper and lower cutoffs for the streamwise wavenumber. For the values of the magnetic and viscous Reynolds numbers accessible in the Helimak, the ideal sinuous mode can be completely stabilized by a small enough viscous Reynolds number and it is relatively insensitive to the magnetic Reynolds number.

3.9 Future work

The next step is to carry out nonlinear simulations of this configuration with the same code used here. The present work provides the basic mode structure to guide the simulations. The linear stability results for some channel flows, such as plane Poiseuille flow and plane Couette flow, do not agree well with the behavior observed in pressure-driven and wall-driven channel flows [81][82]. Therefore, it is important to expand this study to include nonlinear and 3D effects. The extension to a compressible model is also important to include resistive interchange instabilities driven by magnetic curvature.

Table 3.1: Helimak viscoresistive MHD parameters

Toroidal Magnetic Field	$B_\phi = 0.1$ T
Poloidal Magnetic Field	$B_z = 0.01$ T
Half Height	$H = 1.0$ m
Half Width	$L = 0.5$ m
Aspect ratio	$H/L = 2$
Magnetic Field Line Length	$L_\parallel = 20$ m
Argon Density	$n_e = 2 \times 10^{10} - 2 \times 10^{11}$ cm^{-3}
Electron Temperature	$T_e = 10$ eV
Chamber Volume	$V = 13.8$ m^3
Space-Time Scale	$(L, T) = (0.5 \text{ m}, 0.6\ \mu\text{s})$
Magnetic Diffusivity	$\eta/\mu_0 = 30$ m^2/s
Magnetic Reynolds Number	$S = V_A L/(\eta/\mu) = 10^4$
Ion kinematic viscosity	$\nu = 0.3\rho_i^2\nu_i = 0.3$ m^2/s
Reynolds Number	$S_\nu = 10^4$
Bohm Diffusivity	$\chi_e = \frac{1}{16}\frac{T_e}{B} = 6$ m^2/s

Chapter 4

Conclusions

We presented an explanation for Alvénic fluctuations in sheared magnetic field in the LAPD experiment, and a comparison between the evolution of a bounded magnetized plasma jet in the Helimak experiment and the evolution of an unbounded magnetized plasma jet.

4.1 Alfvénic fluctuations in LAPD experiment

The LAPD experiment revealed unexplained transient broad spectrum magnetic fluctuations in an experiment with a region of smooth shear flow [13]. We proposed that these transient dynamics are caused by shear-induced coupling of modes that would be noninteracting in the absence of shear. We evolved the linear system of dynamical equations for the electrostatic potential, axial vector potential and density in terms of Kelvin modes, which are spatial Fourier ansatz with time-dependent phases. The phases of Kelvin modes are time-dependent to reflect the effect of the shear flow. The procedure is done for five sets of typical LAPD parameters.

The evolved fields showed the onset of large electromagnetic fluctuations in the presence of strong shear flow. Dispersion relations showed the

nonresonant coupling of the drift-wave mode with a high-frequency Alfvénic mode. The evolution of perturbation energies reveals electron thermal energy bursts and the appearance of Alfvénic fluctuations. The mechanism revealed in this work has been suggested as a possible cause of electrostatic turbulence that was seen to be correlated with magnetic oscillations near the vessel wall of the Tokamak Chauffage Alfvén Bresilien (TCABR) [83].

The next step for this work is to perform nonlinear simulations to explore the feedback mechanism between nonlinear interactions and the shear flow. Positive feedback could sustain the fluctuations for a long time and lead to turbulence. The goal will be to determine the critical conditions, such as transient fluctuation strength and time scale, for this nonlinear mechanism for the LAPD system, and to generalize the results to other important plasma experiments.

4.2 Evolution of bounded magnetized plasma jet in the Helimak

Magnetized plasma jets in space plasmas are effectively unbounded because the boundaries are so far away compared to the scale of the magnetized jet. However, magnetized jets in the laboratory are more likely to be affected by bounding walls. The objective of this work was to test whether bounded magnetized jets evolve differently than if they were unbounded.

The work presented here is part of a more extensive study published in collaboration with R.B. Dahlburg *et al.* [11]. This work uses as a point

of comparison the results of an earlier work by R.B. Dahlburg *et al.* [4] that characterizes the evolution of an unbounded magnetized plasma jet.

We explored the effect of no-slip walls on a magnetized plasma jet by solving the linear system of equations for the magnetic field and flow field. We spectrally decompose the fields in the bounded direction using a truncated Chebyshev series expansion. The no-slip boundaries are introduced by truncating the series in a way that allows the inclusion of separate boundary condition equations, in what is called the τ-approximation method [74].

Indeed, bounded magnetized plasma jets were found to evolve differently than unbounded jets. The main result was that bounded jets have only one unstable mode; it is a sinuous mode that strongly resembles the ideal sinuous unstable mode of unbounded jets. The unbounded jet additionally has unstable ideal and resistive varicose modes that the bounded jet does not have.

A limitation of this work is that all the nonlinear interactions were neglected. Several studies have shown that some linear stability analyses for channel flows can give results that are very different from experimental results [84] [72]. Therefore, the next step for this study is to evolve the bounded magnetized jet in its full 3D nonlinear form using a 3D code that uses Chebyshev modes along the direction with the no-slip boundaries.

Bibliography

[1] W. Gekelman et al., Rev. Sci. Instrum. **62**, 2875 (1991).

[2] J. C. Perez, W. Horton, R. D. Bengtson, T. Carter, Phys. Plasmas **13**, 055701 (2006).

[3] Horton W, Correa C, Chagelishvili G D, Avsarkisov V S, Lominadze J G, Perez J C, Kim K H, Carter T. A. Phys. Plasmas **16** 092102 (2009).

[4] R. B. Dahlburg, P. Boncinelli, G. Einaudi, Phys. Plasmas **5**, 79 (1998).

[5] V. Carbone, G. Einaudi, P. Veltri, Sol. Phys. **111**, 31 (1987).

[6] R. B. Dahlburg and J. T. Karpen, Astrophys. J. **434**, 766 (1994).

[7] T. Sato, R. J. Walker, J Geophys. Res. **87**, 7453 (1982).

[8] S. Wang, L. C. Lee, C. Q. Wei, S. I Akosofu, Sol. Phys. **117**, 157 (1988).

[9] R. B. Dahlburg, G. Einaudi, T. N. LaRosa, S. N. Shore, Astrophys. J. **568**, 220 (2002).

[10] K. W. Gentle, H. He, Plasma Sci. Technol. **10**, 284 (2008).

[11] R. B. Dahlburg, W. Horton, W. L. Rowan, C. Correa, J. C. Perez, Phys. Plasmas **16**, 072109 (2009).

[12] A. Gibson and the JET Team, Phys. Plasmas **5**, 1839 (1998).

[13] S. E. Sharapov, F. M. Poli, and JET-EFDA Contributors, in Europhysics Conference Abstracts, 35th EPS Conference on Plasma Physics, Hersonis- sos, edited by P. Lalousis and S. Moustaizis European Physical Society, Switzerland, Vol. 32D, p. 4.071 (2008).

[14] W.A. Cooper, Plasma Phys. Control. Fusion **30**, 1805 (1988).

[15] P. C. Liewer, Nucl. Fusion **25**, 543 (1985).

[16] A. J. Wootton, B. A. Carreras, H. Matsumoto, K. McGuire, W. A. Peebles, Ch. P. Ritz, P. W. Terry, S. J. Zweben, Phys. Fluids B **2**, 2879 (1990).

[17] W. Horton, J. C. Perez, T. Carter, R. Bengston, Phys. Plasmas **12**, 022303 (2005).

[18] S. Zhou, W. W. Heidbrink, H. Boehmer, R. McWilliams, T. A. Carter, S. Vincena, S. Tripathi, B. Van Compernolle, Phys. Plasmas **19**, 055904 (2012).

[19] B. Friedman, T.A. Carter Phys. Rev. Lett. **113**, 025003 (2014).

[20] P. Popovich, M. V. Umansky, T. A. Carter, B. Friedman, Phys. of Plasmas **17**, 102107 (2010).

[21] B. Friedman, T. A. Carter, M. V. Umansky, D. Schaffner, B. Dudson **19**, 102307 (2012).

[22] Lord Kelvin, Philos. Mag. **24**, Ser.5, 188, (1887).

[23] W. McF. Orr, Proc. R. Irish Acad. Sci. **A 27**, 9 (1907).

[24] W. McF. Orr, Proc. R. Irish Acad. Sci. **A 27**, 69 (1907).

[25] S. C. Reddy, P. J. Schmid, D. S. Henningson, SIAM J. Appl. Math. **53**, 15 (1993).

[26] P. W. Terry, Rev. Mod. Phys. **72**, 109 (2000).

[27] P. H. Diamond, S. I. Itoh, K. Itoh, T. S. Hahm, Plasma Phys. Control. Fusion **47**, R35 (2005).

[28] Lord Rayleigh, Proc. Lond. Math. Soc. **11**, 57, (1880).

[29] P. J. Schmid, D. S. Henningson, *Stability and Transition in Shear Flows*, Springer-Verlag, New York (2001).

[30] W. O. Criminale, T. L. Jackson, R. D. Jolin, *Theory and Computation of Hydrodynamic Stability*, Cambridge University Press, Cambridge (2003).

[31] L. Trefethen, M. Embree, *Spectra and Pseudospectra: the Behavior of Nonnormal Matrices and Operators*, Princeton University Press, Princeton (2005).

[32] P. J. Schmid, Annu. Rev. Fluid Mech. **39**, 129 (2007).

[33] W. O. Criminale, P. G. Drazin, Studies in Appl. Math. **83**, 123 (1990).

[34] L. H Gustavsson, J. Fluid Mech. **224**, 241 (1991).

[35] K. M. Butler, B. F. Farrell, Phys. Fluids A **4**, 1637 (1992).

[36] S. A. Balbus, J. F. Hawley, Astroph.Journal **376**, 214 (1991).

[37] Y. Nakagawa, M. Sekiya, Monthly Notices of the Royal Astronomical Society **256**, 685 (1992).

[38] S. C. Reddy, D. S. Henningson, J.Fluid Mech **252**, 209 (1993).

[39] G. D. Chagelishvili, T. S. Hristov, R. G. Chanishvili, J. G. Lominadze, Phys. Rev. E **47**, 366 (1993).

[40] G. D. Chagelishvili, A. G. Tevzadze, G. Bodo, S. S.Moiseev, Phys. Rev. Lett. **79**, 3178 (1997).

[41] A. G. Tevzadze, Phys. Plasmas **5** 1557 (1998).

[42] G. D. Chagelishvili, R. G. Chanishvili, J. G. Lominadze, A. G. Tevzadze, Phys. Plasmas **4**, 259 (1997).

[43] G. D. Chagelishvili, *Sound-Flow Interactions (Lecture Notes in Physics)*, edited by Y. Auregan, A. Maurel, V. Pagneux, J.F. Pinton, Springer, Berlin (2002)

[44] M. T. Landahl, J. Fluid Mech. **98**, 243 (1980).

[45] G. D. Chagelishvili, R. G. Chanishvili, J. G. Lominadze, JETP Lett. **63**, 543 (1996).

[46] B. B. Kadomtsev, O. P. Pogutse, in *Reviews of Plasma Physics, Volume 5*, edited by Acad. M. A. Leontovich. Consultants Bureau, New York (1970)

[47] T. A. Carter, J. E. Maggs, Phys. Plasmas **16**, 012304 (2009).

[48] G. D. Chagelishvili, A. D. Rogava, D. G. Tsiklauri, Phys. Rev. E **53**, 6028 (1996).

[49] G. T. Gogoberidze, G. D. Chagelishvili, R. Z. Sagdeev, J. G. Lominadze, Phys. Plasmas **11**, 4672 (2004).

[50] L. Boberg, U. Brosa, Z. Naturforsch., Teil A., **43**, 697 (1988).

[51] L. N. Trefethen, A. E. Trefethen, S. C. Reddy, T. A. Driscoll, Science **261**, 578 (1993).

[52] M. V. Morkovin, *Instabilities and Turbulence in Engineering flows*, edited by D. E. Ashpis, T. B. Gatski and R. S. Hirsh, Kluwer Academic Press, New York (1993).

[53] T. Gebhardt, S. Grossmann, Phys. Rev. E **50(5)**, 3705 (1994).

[54] D. S. Henningson, S. C. Reddy, Phys. Fluids **6**, 1396 (1994).

[55] J. S. Baggett, T. A. Driscoll, L. N. Trefethen, Phys. Fluids **7**, 833 (1994).

[56] S. Grossmann, Rev. Mod. Phys. **72**, 603 (2000).

[57] E. Reshotko, Phys. Fluids **13**, 1067 (2001).

[58] S. J. Chapman, J. Fluid Mech. **451**, 35 (2002).

[59] G. D. Chagelishvili, R. G. Chanishvili, T. S. Hristov, J. G. Lominadze, JETP **94**, 434 (2002).

[60] D. Rempfer, Annu. Rev. Fluid Mech. **35**, 229 (2003).

[61] Horton, W., *Turbulent Transport in Magnetized Plasmas*, World Scientific, Singapore (2012).

[62] J. T. Mendona, S. Benkadda, Phys. Plasmas **19**, 082316 (2012).

[63] Mikhailenko, V. S., Mikhailenko, V. V., Stepanov, K. N., Azarenkov, N. A., Phys. Plasmas **15** (7), 072102 (2008).

[64] Ratushnaya, V., Ravi S., Europhysics Letters **108.5**, 55001 (2014).

[65] Squire, J., Bhattacharjee, A., Bulletin of the American Physical Society **59** (2014).

[67] J. C. Perez, W. Horton, K. Gentle, W. L. Rowan, K. Lee, R. B. Dahlburg, Phys. Plasmas **13**, 032101 (2006).

[68] G. Einaudi, P. Boncinelli, R. B. Dahlburg, J. T. Karpen, J. Geophys. Res. **104** 521 (1999).

[69] R. B. Paris, W. NC. Sy, Phys. Fluids **26**, 2966 (1983).

[70] P. R. Nachtsheim, E. Reshotko, NASA Technical Note d3144 , National Aeronautics and Space Administration, Washington D.C. 20546 **123456** (1965).

[71] S. A. Orszag, J. Fluid Mech. **50**, 689 (1971).

[72] R. B. Dahlburg, T. A. Zang, D. Montgomery, M. Y. Hussaini, Proc. Nat. Acad. Sci USA. **80**, 5798 (1983).

[73] R. B. Dahlburg, T. A. Zang, D. Montgomery, J. Fluid Mech. **169**, 71 (1986).

[74] C. Lanczos, *Applied Analysis*, Prentice-Hall, NY (1956).

[75] J. Gary, R. Helgason, J. Comp. Phys **5**, 169 (1970).

[76] H. B. Squire, Proc. R. Soc. A **142**, 621 (1933).

[77] R. B. Dahlburg, J. T. Karpen, J. Geophys. Res. **100**, 23489 (1985).

[78] N. Seehafer, J. Schumacher, Phys. Plasmas **5**, 2363 (1998).

[79] D. W. Hughes, S. M. Tobias, Proc. R. Soc. London Ser. A **457**, 1365 (2001).

[80] R. B. Dahlburg, P. Boncinelli, G. Einaudi, Phys. Plasmas **4**, 1213 (1997).

[81] P. G. Drazin, W. H. Reid, *Hydrodynamic stability*, Cambridge University Press, Cambridge (1981).

[82] D. Montgomery, Physica Scripta **T2/2**, 506 (1982).

[83] Z. O. Guimarães-Filho, G. Z. dos Santos Lima, I. L. Caldas, R. L. Viana, I. C. Nascimento, Yu. K. Kuznetsov, Journal of Physics: Conference Series **246** (2010).

[84] P. G. Drazin, J. Fluid Mech. **8**, 130 (1960).

Vita

Cynthia Elizabeth Correa was born in Durango, Mexico. She received a Bachelor of Arts degree in Physics from Harvard College in May, 2004. She discovered Plasma Physics during a year spent as a researcher for Dr. Carlos Ordonez at the University of North Texas. Cynthia joined Dr. Wendell Horton's group at the University of Texas at Austin in August, 2008.

Permanent address: cynthiacorrea@gmail.com

This dissertation was typeset with LaTeX[†] by the author.

[†]LaTeX is a document preparation system developed by Leslie Lamport as a special version of Donald Knuth's TeX Program.